



EMME-CARE

EASTERN MEDITERRANEAN
MIDDLE EAST – CLIMATE &
ATMOSPHERE RESEARCH CENTRE

HORIZON 2020 – WIDESPREAD-2018-01-TEAMINGPHASE2
EMME-CARE | GRANT No. 856612

D6.3: Report on emission analyses for the EMME region

August 2023



This project has received funding
from the European Union's Horizon 2020 research
and innovation programme under grant agreement
No. 856612 and the Cyprus Government



Deliverable Number	Deliverable Title	Lead Beneficiary	Type	Dissemination Level	Due Date (in months)
D6.3	Report on emission analyses for the EMME region	CEA	Report	Internal	48

Version	Date	Changed page(s)	Cause of change	Partner
V1	15/07/2023	Initial version		CEA
V2	25/07/2023	Final version	Review by coordination	Cyl

Disclaimer: The information in this document is subject to change without notice. Company or product names mentioned in this document may be trademarks or registered trademarks of their respective companies.

All rights reserved

The document is proprietary of the EMME-CARE Consortium Members. No copying or distributing in any form or by any means is allowed without the prior written agreement of the owner of the property rights.

This document reflects only the authors' view. The European Community is not liable for any use that may be made for the information contained herein.

Table of Contents

Contents

Introduction.....	4
1. Explanation of the work carried out by the beneficiaries and Overview of the progress.....	5
1.1. Objectives (Short description/summary)	5
1.2. Ground-based and satellite CO₂ data assimilated into the EMME inverse modelling configuration	6
1.2.1 Estimates of daily CO ₂ emissions for atmospheric analysis	6
1.3. Inverse model system to include the assimilation of space-borne measurements of air pollutants	8
1.3.1 Atmospheric analysis of CH ₄ emissions using a global inversion.....	8
1.3.2 Atmospheric analysis of CH ₄ emissions compared to inventories	10
1.3.3 Atmospheric analysis of CH ₄ emissions over main extraction basins.....	13
1.3.4 Atmospheric analysis of NO _x emissions using a global inversion.....	14
1.3.5 Atmospheric analysis of NO _x emissions using a regional inversion.....	17
1.3.6 Atmospheric analysis of SO ₂ emissions using a global inversion.....	19
1.3.7 Atmospheric analysis of NH ₃ emissions using a global inversion.....	21
1.4. Establishment of an emission analysis system at Cyl, based on ground-based and satellite data and first applications in atmospheric modelling	22
1.4.1 Establishment of an emission analysis system at Cyl, based on ground-based and satellite data.....	22
1.4.2. Inventory Source Comparison	23
1.4.3. Sectoral Emission Analysis	26
1.4.4. Gridded emission information modelling applications	28
1.4.5. Model performance	31
1.4.6. Emission analysis system.....	32
2. Key aspects of the implementation of the project.....	37
2.1. Autonomy, Decision-making.....	37
2.2. Complementary funding	37
3. Strategy for the upcoming period.....	37
4. Publications	37
5. References	38

Introduction

The **WP6** objectives are to develop capability, enhance environmental knowledge and research through earth system modelling, forecasting, risk analysis and scenario calculations. This WP includes inverse emission modelling, pollution and hazard forecasting, climate analyses and projections through regional downscaling. This report is focused on the inverse modelling of pollutant and greenhouse gases (GHG) emissions in the EMME region, using atmospheric concentration measurements collected mainly from satellites in the absence of dense in-situ networks over the region, except for the new stations installed in Cyprus. **This deliverable describes the results obtained at month 48 for the task 6.3 ‘emissions analysis in the EMME region’ led by CEA with contribution of MPG.**

The Eastern Mediterranean and the Middle East (EMME) region is characterized by high background tropospheric ozone concentrations (Lelieveld et al., 2002, 2009; Zanis et al., 2014), since it is affected by polluted air masses from various sources such as the eastern and central Europe, and the Middle East (Lelieveld et al., 2002; Gerasopoulos et al., 2005; Kalabokas et al., 2008; Kanakidou et al., 2011).

The EMME region is a large global emitter of greenhouse gases and pollutants, mainly from the energy and industry sector. The energy demand per capita is high, being driven in particular by cooling requirements in buildings during the hot season. Most of the power supply is from fossil fuel burning, mainly gas which is extracted in many of the countries of the region. In addition, there are fugitive emissions of methane, a powerful greenhouse gas relative to CO₂, related to leaks during the extraction, storage, flaring and storage or liquefaction of natural gas.

In the following, we focus on CO₂, CH₄, NO_x, SO₂ and NH₃. These species have been observed by different satellites since the late 2000s. All satellite measurements are collected using passive spectrometers used to retrieve column concentrations during clear-sky periods using radiative transfer models. A revolution in the sampling of the atmosphere came with the TROPOMI instrument on Sentinel 5P launched in 2018 by the European Space Agency, which collects daily images of column CH₄, CO, NO_x, SO₂ concentration over the whole globe. The low cloudiness of the EMME region makes it a good candidate for constraining emissions using satellites such as TROPOMI. On the other hand, variable desert albedo and high aerosols loads in the atmosphere decrease the quality of satellite retrievals in some instances for the EMME region, and many emissions are located on the coast or in complex terrain, where the quality of measurements and local atmospheric circulations complicate the inference of emissions.

In the following, **we describe the assimilation of atmospheric composition measurements in atmospheric transport models at different spatial resolution to infer the emissions of CO₂, CH₄, NO_x, SO₂ and NH₃, performed in Task 6.3.**

These results have been published in 4 peer reviewed publications since the start of the EMME CARE project (see section publications)

1.Explanation of the work carried out by the beneficiaries and Overview of the progress

In line with the [Annex 1](#) to the Grant Agreement, the work performed in [Task 6.3](#) consisted to design, calibrate and apply atmospheric inversions models to constrain the emissions of greenhouse gases and pollutants over the EMME regions and / or specific sub-regions and countries. We used global atmospheric inversions constrained by satellite and in-situ stations for CH₄, global inversions with a chemistry transport model for emissions of short-lived reactive gases NO_x, SO₂ and NH₃, and regional inversions using high resolution wind fields to infer CH₄ emissions from large point sources, from main extraction basins of oil and gas in the Persian Gulf area and NO_x emissions in Egypt, Qatar and Cyprus.

- The **first key result** is an original analysis combining a priori inventories and global CH₄ observations from GOSAT to **explain the regional changes of CH₄ emissions and sinks during the years 2020 and 2021**, when the global atmospheric growth rate of CH₄ reached a record high value at about 15 ppb per year. This result was published in Nature ([Peng et al., 2022](#)).
- The **second key result** is an analysis of **intense localised CH₄ emissions from leaks detected by the TROPOMI satellite over the globe and the EMME region**, published in Science ([Lauvaux et al. 2022](#)).
- The **third key result** is **regional CH₄ emissions from fossil gas and oil extraction activity in Kuwait, Southern Iraq, North Western Iran** obtained from regional inversions using TROPOMI images ([Peng et al. 2022](#)).
- The **fourth key result** is the NO_x emission budget of the years 2019 to 2021 using the LMDZ INCA chemistry model run in a data assimilation mode using OMI and TROPOMI data, and **regional maps of NO_x emissions for Egypt, Qatar and Cyprus** using a high-resolution transport and chemistry inversion. These latter results have been published in ACP ([Rey Pommier et al. 2022](#)) for Egypt and in ACPD for Qatar ([Rey Pommier et al. 2023](#)).
- The **fifth key result**, for CO₂, is the results of a new dynamic inventory of fossil CO₂ emissions covering the period 2019 to 2023. The data are daily on a grid of 1 km.

1.1. Objectives (Short description/summary)

In the DoA, [task 6.3](#) listed the following subtasks, with the overarching objective to improve emissions estimates of greenhouse gases and pollutants over the EMME region. This task is divided into three sub-tasks

Task 6.3a Ground-based and satellite CO₂ data assimilated into the EMME inverse modelling configuration.

Task 6.3b Inverse model system to include the assimilation of space-borne measurements of air pollutants (e.g. CO, NO₂), together with anthropogenic CO₂ emissions by means of parameter corrections in the emission model.

Task 6.3c Establishment of an emission analysis system at Cyl, based on ground-based and satellite data and first applications in atmospheric modelling, enhanced by a boost project on emissions with ARIA Technologies.

The work performed by CEA, MPG and CYI in those tasks has been extended to the analysis of CH₄, SO₂ and NH₃ emissions using a global inversion model based on the LMDZ INCA chemistry aerosol model and a 4DVAR inversion system for CH₄. We have hired two postdoctoral researchers full time on the project at CEA, K. Tibrewal for the comparison between CH₄ inversions and a suite of bottom up inventories, and S. Halder for NO_x inversions. One postdoc was hired on the task and left after 12 months, Z. Tzsompa-Soza after contributing to a publication. One additional research fellow was hired for CH₄ emissions. One PhD student A. Rey Pommier was hired by LSCE and CYI (joint PhD) and has worked on NO_x emissions

1.2. Ground-based and satellite CO₂ data assimilated into the EMME inverse modelling configuration

1.2.1 Estimates of daily CO₂ emissions for atmospheric analysis

This work relates to the subtask **T6.3a** for which high quality bottom-up near real time CO₂ emissions inventories needed to be compiled as a prior of top down inversions. In parallel, a regional configuration of the CO₂ inversion model based on the CHIMERE_CIF system has been designed but it has not yet been applied to the inversion of OCO₂ satellite data. Instead, global analysis from LMDZ-CIF inversions have been performed.

We describe in the following the bottom-up near real time dynamic emission inventory of fossil fuel CO₂ emissions for the EMME region developed by using near real time daily activity data for more than 47 countries and downscaled using point sources (power plants), industries locations and the spatial activity patterns for 6 sectors: power generation, industry, transportation, residential direct CO₂ emissions, shipping and aviation. The figures below represent emissions maps over the EMME region at 10 km resolution for all sectors and specific sectors, as well as year on year changes from 2019.

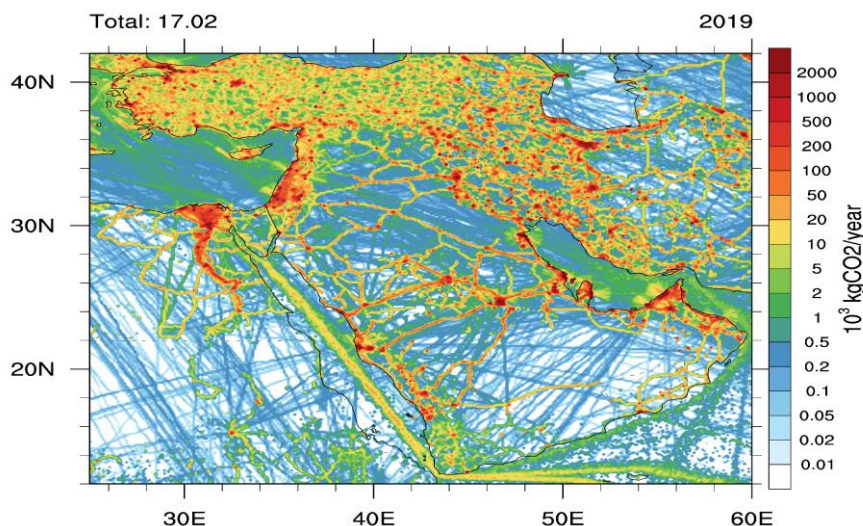


Fig 1.2.1-1. Map of CO₂ emissions from all sectors in 2019

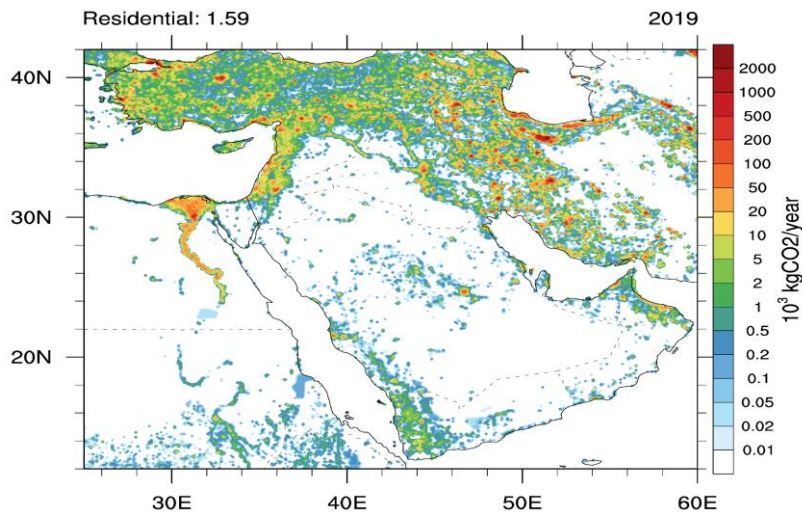


Fig 1.2.1-2. Map of CO₂ emissions from the residential sector direct emissions in 2019

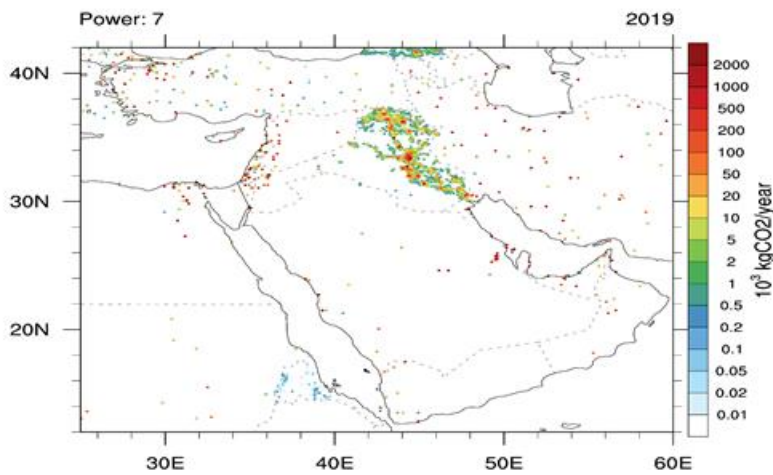


Fig 1.2.1-3. Map of CO₂ emissions from the power sector direct emissions in 2019

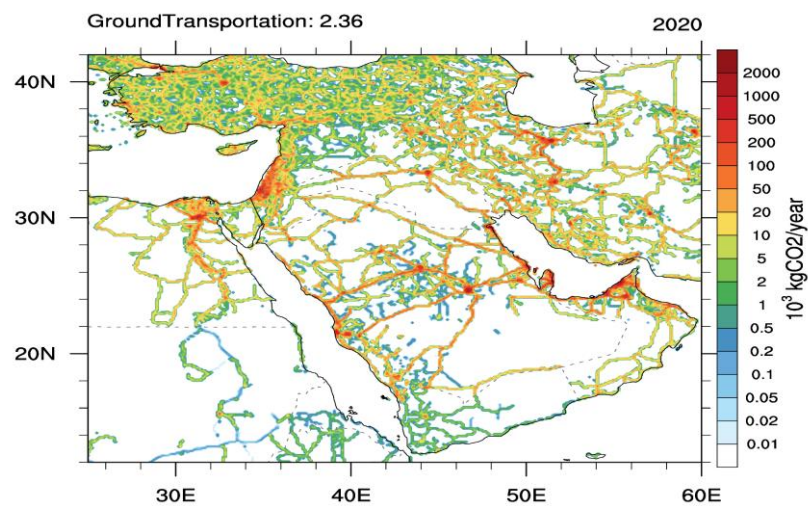


Fig 1.2.1-4. Map of CO₂ emissions from the ground transportation sector direct emissions in 2019

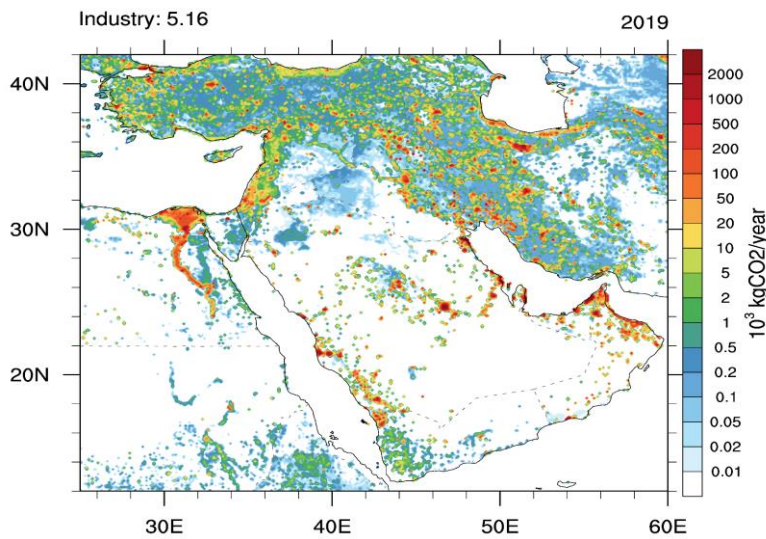


Fig 1.2.1-5. Map of CO₂ emissions from the industry sector direct emissions in 2019

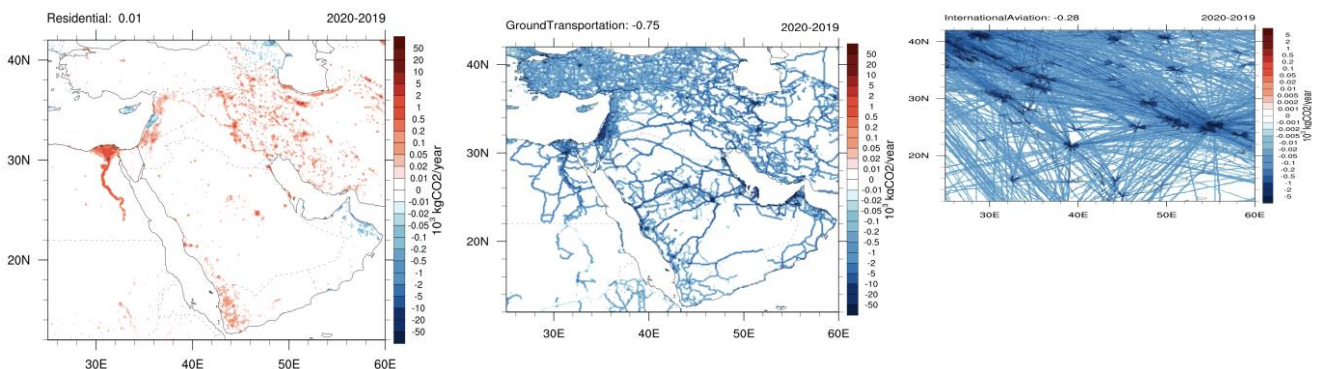


Fig. 1.2.1-6 Difference of emissions between 2020 and 2019 from the COVID pandemics for selected sectors

1.3. Inverse model system to include the assimilation of space-borne measurements of air pollutants

1.3.1 Atmospheric analysis of CH₄ emissions using a global inversion

This work extends the [task 6.3](#) to the analysis of **CH₄ emissions using a global inversion model PYVAR-LMDZ-SACS** (Locatelli et al., 2015; Yin et al., 2021), focusing on the recent emission changes from 2019 to 2021. The methane growth rates in the atmosphere were 15.2 ± 0.4 and 17.7 ± 0.5 parts per billion per year (ppb yr⁻¹) in 2020 and 2021, the highest since systematic measurements started in early 1980s by NOAA's Global Monitoring Laboratory (https://gml.noaa.gov/ccgg/trends_ch4).

To understand the drivers behind the extremely high methane growth, we applied PYVAR-LMDZ-SACS to infer the emission changes and identify regions with large emission increases (Peng et al., 2022). An ensemble of six inversions was performed, which assimilated three different observation datasets (surface network, GOSAT XCH₄ NIES retrievals, and GOSAT XCH₄ University of Leicester retrievals) and applied two versions of the transport model LMDZ (**Table 1.3.1-1**). This allows us to test the consistency of the flux change patterns inferred from different types of measurements while accounting for some of the uncertainties due to imperfect representation of atmospheric mixing. The inversions were performed at the spatial resolution of 1.9° in latitude by 3.75° in longitude and the temporal resolution of 8 days. As such, we aim to build a tracking system of global methane emissions at a latency of 1 year.

Table 1.3.1-1 Configurations of the ensemble of six global CH₄ inversions

Inversions	Observations assimilated	Transport model versions
Surf_a	Surface networks	LMDZ AR3 version
Surf_b	Surface networks	LMDZ AR6 version
GSNIES_a	GOSAT XCH ₄ NIES full physics retrievals	LMDZ AR3 version
GSNIES_b	GOSAT XCH ₄ NIES full physics retrievals	LMDZ AR6 version
GSUoL_a	GOSAT XCH ₄ University of Leicester proxy retrievals	LMDZ AR3 version
GSUoL_b	GOSAT XCH ₄ University of Leicester proxy retrievals	LMDZ AR6 version

The annual mean global CH₄ emissions were 551.1 ± 1.3 Tg CH₄ yr⁻¹, 571.4 ± 8.9 Tg CH₄ yr⁻¹ and 575.9 ± 3.1 Tg CH₄ yr⁻¹ for 2019, 2020 and 2021, respectively, based on the ensemble of six inversions. Emissions from the EMME region represent about 3-4% of global emissions, amounting to 18.7 ± 9.9 Tg CH₄ yr⁻¹, 18.8 ± 10.0 Tg CH₄ yr⁻¹ and 20.3 ± 11.2 Tg CH₄ yr⁻¹ for 2019, 2020 and 2021, respectively (Fig 1.3.1-1 and Fig. 1.3.1-2). Emissions in the EMME region are dominated by anthropogenic sources, mostly from oil and gas production (see section 1.3.2 for details). Iran, Turkey, Iraq, Egypt, Saudi Arabia are the major emitting countries of this region (Fig. 1.3.1-2), together contributing 87-89% of the regional emissions.

Compared to 2019, the emissions of CH₄ increased by 20.3 ± 9.9 Tg CH₄ yr⁻¹ and 24.8 ± 3.1 Tg CH₄ yr⁻¹ globally in 2020 and 2021, respectively. Most of the emission increases were attributed to the northern tropical region (0°-30°N), by 16.2 ± 8.3 Tg CH₄ yr⁻¹ and 23.2 ± 4.0 Tg CH₄ yr⁻¹ in 2020 and 2021, respectively, likely due to strong emission enhancements from biogenic sources. The EMME region, partly located in the northern tropics though, had a small net contribution to the global and zonal emission increases (0.2 ± 1.0 Tg CH₄ yr⁻¹ and 1.7 ± 1.7 Tg CH₄ yr⁻¹ in 2020 and 2021, respectively). Saudi Arabia (for both 2020 and 2021) and Iran (for 2021) were the two countries with the largest contribution to the emission increases (Fig 1.3.1-1 and Fig 1.3.1-2).

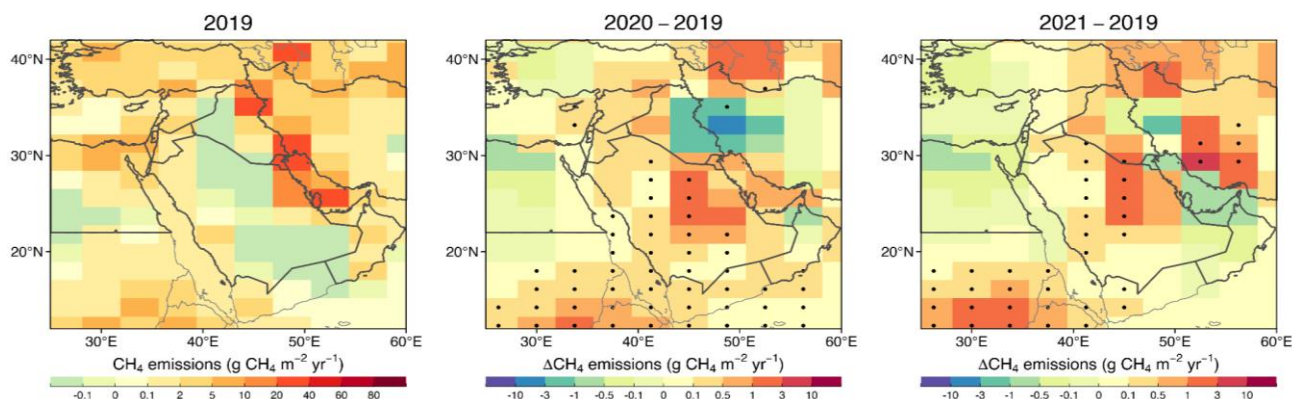


Fig 1.3.1-1. The spatial patterns of annual mean posterior CH₄ emissions over the EMME region in 2019 (left) and the emission changes in 2020 (middle) and 2021 (right). The annual mean emissions and emission changes are averaged from the ensemble of six global inversions listed in Table 1.3.1-1. Black dots indicate model grids where the directions of emission changes agree among all six inversions.

It should be noted that among the six inversions, there is a large spread in the estimates of emissions and their changes at the regional scale and the country level, especially between the inversions constrained by surface observations and those constrained by GOSAT observations (Fig 1.3.1-2). Part of the disagreement is due to lack of surface observations in the EMME region (see Supplementary Fig. 12 in Peng et al. 2022). The coarse spatial resolution of the global inversions also prevents accurate emission estimation for small countries in this region. In the next step, we will apply a high-resolution regional inversion model, together with TROPOMI XCH₄ data and fine-scale emission inventories for better characterization of the CH₄ emissions in this region.

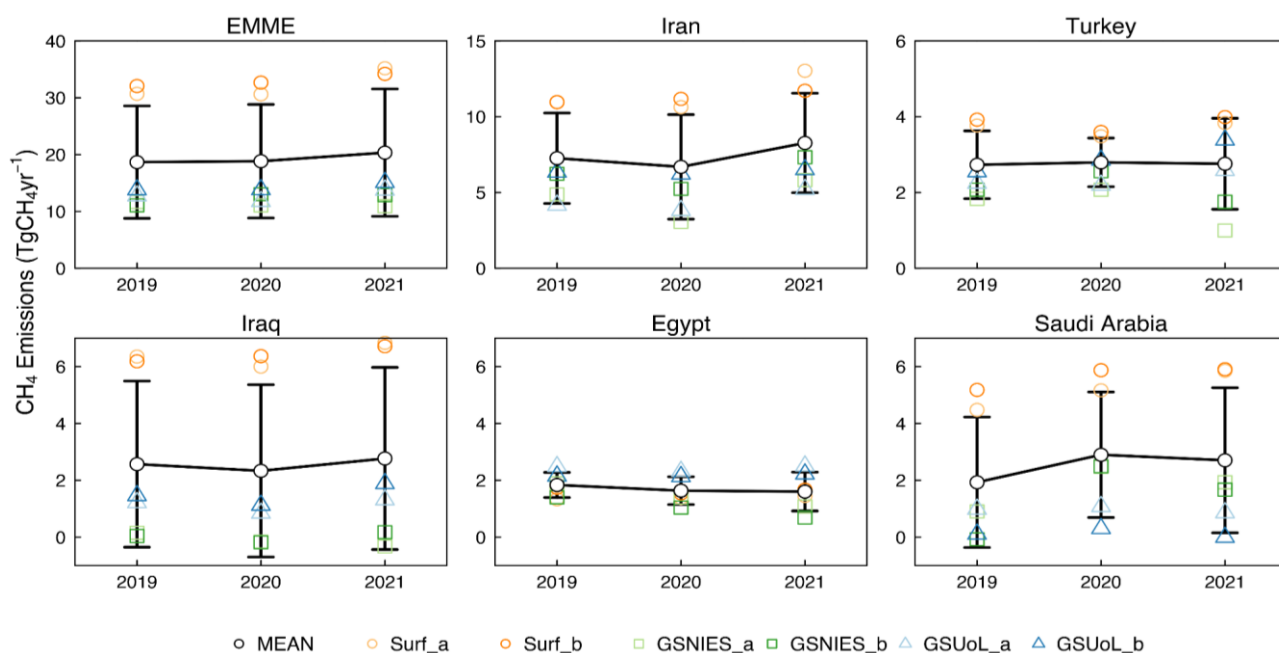


Fig 1.3.1-2. Changes in CH₄ emissions over the EMME region from 2019 to 2021 derived from an ensemble of six inversions. Emission changes for the major CH₄ emitting countries (Iran, Turkey, Iraq, Egypt and Saudi Arabia) are also presented. Error bars represent ± 1 standard deviation.

1.3.2 Atmospheric analysis of CH₄ emissions compared to inventories

Exploitation of fossil fuels, which consists of exploration, production and distribution of fossil fuels (coal, oil and gas) is a significant contributor to methane emissions for the EMME region. Most countries within this region (i.e., Greece, Iraq, Cyprus, Lebanon, Jordan, Israel, Saudi Arabia, Egypt, Kuwait, Oman, Qatar and United Arab Emirates) have committed to reducing methane under the Global Methane Pledge. In regard to this, fossil fuel sector is regarded to be a key potential sector for cost-effective mitigation. Using a set of global bottom-up inventories and a new ensemble of global inversion results updated to 2020 by the Global Carbon Project (<https://www.globalcarbonproject.org/>), we present the range of methane emissions from the fossil sector over this region during the last decade (2011-2020).

The top-down models include 1) a new ensemble of 12 global inversions spanning from the year 2000 to 2020 (10 surface-based inversions for the period 2000-2020 and two satellite-based inversions for the period 2010-2020); and 2) 2019-2020 country-wide estimates of CH₄ ultra-emissions from oil and gas sources based on the TROPOMI satellite data. The ensemble of bottom-up inventories consists of national submissions to UNFCCC compiled from different sources and different global inventories (Deng et al., 2022), including the Community Emissions Data System (CEDS; (O'Rourke et al., 2021), the Emissions Database for Global Atmospheric Research (EDGARv6; (Crippa et al., 2021), the Greenhouse gas and Air pollutant Interactions and Synergies (GAINS; Höglund-Isaksson et al., 2020), the Global Fuel Exploitation Inventory (GFEI; Scarpelli et al., 2022), International Energy Agency (IEA; International Energy Agency, 2021) and the U.S. Environmental Agency (EPA; USEPA 2021).

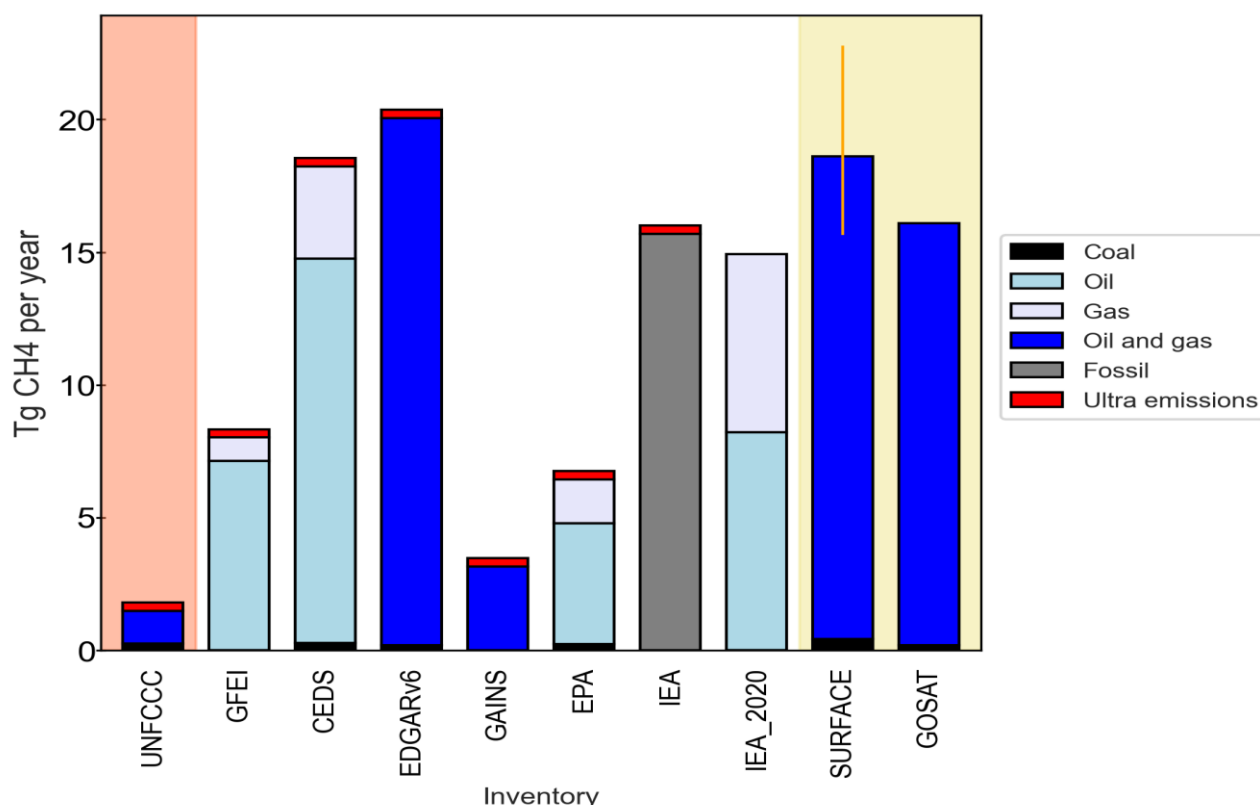


Fig 1.3.2-1. Average fugitive CH₄ emissions (2011-2020) from fossil fuels across bottom-up and top-down approaches over countries from the EMME region. Inversions on the right are from surface network and GOSAT satellite products. UNFCCC are the interpolated estimate from countries national communications and Biennial update reports, showing much less emissions than in other inventories and inversions.

The EMME region comprises 15 countries including Cyprus, Egypt, Greece, Iran, Iraq, Israel, Jordan, Kuwait, Lebanon, Oman, Qatar, Saudi Arabia, Syria, Turkey and United Arab Emirates. These countries collectively emitted around 13 (3-20) Tg yr⁻¹ (bottom-up excluding UNFCCC) and 18 (16-23) Tg yr⁻¹ (top-down) during 2011-2020, with almost all emissions from the oil and gas sector and negligible emissions from the coal sector (**Figure 1.3.2-1**). Over the last decade, the average annual emissions from the total fossil sector were ~45% higher in global inversions (SURFACE and GOSAT) compared to bottom-up estimates. While the discrepancy between the mean estimates from SURFACE (19 Tg yr⁻¹) and GOSAT (16 Tg yr⁻¹) lies within 15%, there exists much larger disagreement among the bottom-up estimates. GAINS reported the lowest emissions, with estimates nearly 70% lower than the mean of bottom-up inventories followed by EPA and GFEI which reported ~60% lower emissions. On the other hand, estimates from IEA and IEA_2020 are ~20% higher and from CEDS and EDGARv6 are ~50% higher than bottom-up mean. Compared to global inversions, estimates from GAINS, EPA and GFEI were at least 50% lower while estimates from IEA, IEA_2020, CEDS and EDGARv6 showed good agreement (within ±10%).

Country	Years reported	UNFCCC report type*
Iran	1994, 2000, 2010	NC
Iraq	1997	NC
Saudi Arabia	1990,2000,2010,2016	NC
United Arab Emirates	1994, 2000, 2005	NC

Country	Years reported	UNFCCC report type*
Iran	1994, 2000, 2010	NC
Iraq	1997	NC
Qatar	2007	NC
Egypt	1990, 2000, 2015	NC/BUR
Oman	1994, 2000, 2015	NC/BUR

*NC: National Communications | BUR: Biennial Update Reports

Table 1.3.2-1. Summary of methane anthropogenic emissions submitted to UNFCCC for major emitting countries in the EMME region

Average estimates from UNFCCC (1.8 Tg yr⁻¹) are at least 80% lower than the mean from other bottom-up inventories and global inversions. These are not included with the bottom-up mean above due to incomplete emissions information for most of the countries. Only Turkey, Greece and Cyprus have reported annual emissions in form of National Inventory Reports (NIR) submitted each year to UNFCCC. However, these countries represent <5% of total emissions from this region. Out of the major emitting countries within this region (**Table 1.3.2-1**), only Saudi Arabia, Egypt and Oman provide an estimate for a year in the last decade. The leading emitters, Iran and Iraq, contributing almost ~50% to the total emissions from this region, do not have any estimate during the last decade. For Iraq the latest estimate is for the year 1997.

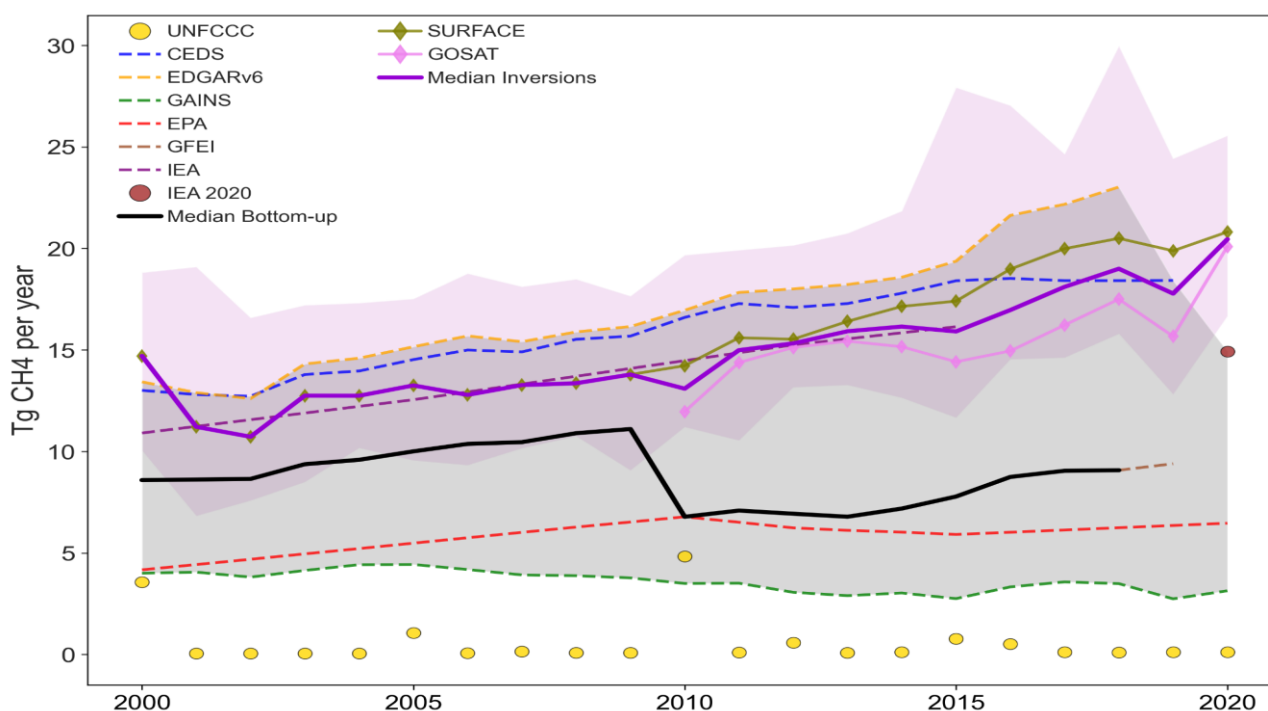


Fig 1.3.2-2. Time series of CH₄ emissions (2000-2020) from fossil sector across bottom-up and top-down approaches over the EMME region. The shaded region represents the spread of the bottom-up inventories (grey) and inversions (pink).

In regard to the emissions trajectories from 2000 to 2020 (**Figure 1.3.2-2**), median of inversions show a steeper trend than the bottom-up median. This is mainly driven by the higher incline in the inversion estimates during the last decade (2011-2020). Both bottom-up (0.10±0.12 Tg yr⁻²) and inversions (0.10±0.11 Tg yr⁻²) median show similar trend during 2000-2010. However, during 2011-2020, inversions (0.54±0.08 Tg yr⁻²) show almost five times steeper increase in emissions than the median of bottom-up inventories (0.12±0.11 Tg yr⁻²). Similar to the magnitudes, trends in SURFACE and GOSAT

inversions are also similar, however disagreements exist among the bottom-up inventories. GAINS is the only bottom-up inventory reporting a declining trend ($-0.07 \pm 0.01 \text{ Tg yr}^{-2}$) during 2000-2020. EPA show a modest increase of ($0.09 \pm 0.02 \text{ Tg yr}^{-2}$) followed by steeper trends from CEDS ($0.34 \pm 0.02 \text{ Tg yr}^{-2}$), IEA ($0.36 \pm 0.01 \text{ Tg yr}^{-2}$) and GFEI ($0.33 \pm 0.04 \text{ Tg yr}^{-2}$) during 2000-2020. EDGARv6 reports the highest incline ($0.52 \pm 0.03 \text{ Tg yr}^{-2}$) among the bottom-up inventories during 2000-2020.

1.3.3 Atmospheric analysis of CH₄ emissions over main extraction basins

Here we analyse the CH₄ emissions over the major fossil fuels basins in the EMME region (**Fig. 1.3.3-1**). Unlike the inversions presented in the previous section which are based on global inversions, these inversions are carried out at a regional level using the bias-corrected methane column mixing ratios derived from the spaceborne instrument TROPOMI on board of the Sentinel 5P satellite by Kayrros. The inversions are carried out for three years, 2019 - 2021 to provide the total CH₄ over these basins. Cumulatively these basins emitted an average of 4.3 (3.4-5.1) Tg yr⁻¹ during 2019-2021, which represents nearly a quarter (25%) of the total CH₄ emissions from the fossil sector over this region (discussed in [section 1.3.2](#)).

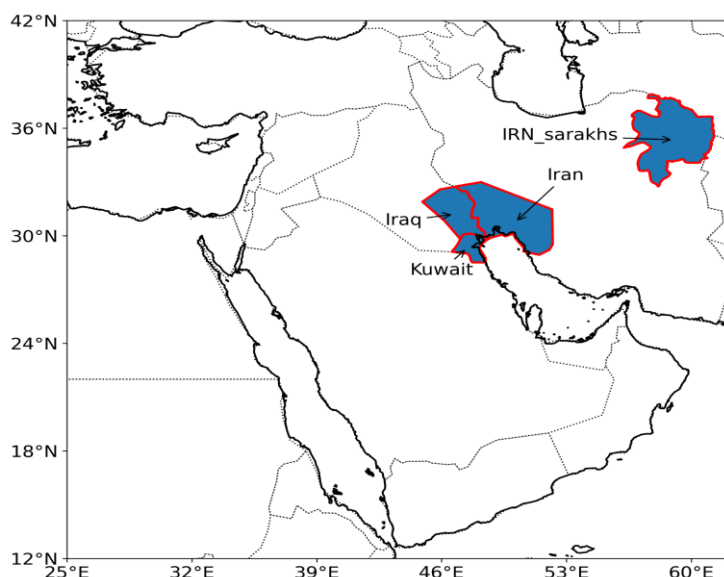


Fig 1.3.3-1. Location of basins covered by Kayrros inversions of TROPOMI images

We compare these regional inversions using gridded emissions of bottom-up inventories (GFEIv2, CEDS, GAINS and EDGARv7) (**Fig 1.3.3-2**).

- **For Iran**, the mean emissions from bottom-up inventories is 70% higher than the regional inversions during 2019-2021, with a poorer agreement in emissions in the year 2021. This discrepancy is mostly driven by emissions from EDGARv7 and CEDS which are around double and 70% higher than regional inversions respectively. Emissions from GFEIv2 are slightly higher (40%) than regional inversions, while GAINS shows good agreement.
- **For Iraq**, the mean emissions from bottom-up inventories is almost double than the regional inversions during 2019-2021, with a better agreement in emissions in the year 2021. This discrepancy is mostly driven by emissions from GAINS which are 4 times higher than regional inversions followed by higher emissions from EDGARv7 (55%) and GFEIv2 (75%). Emissions from CEDS show relatively better agreement with the average emissions being 20% higher than regional inversions.

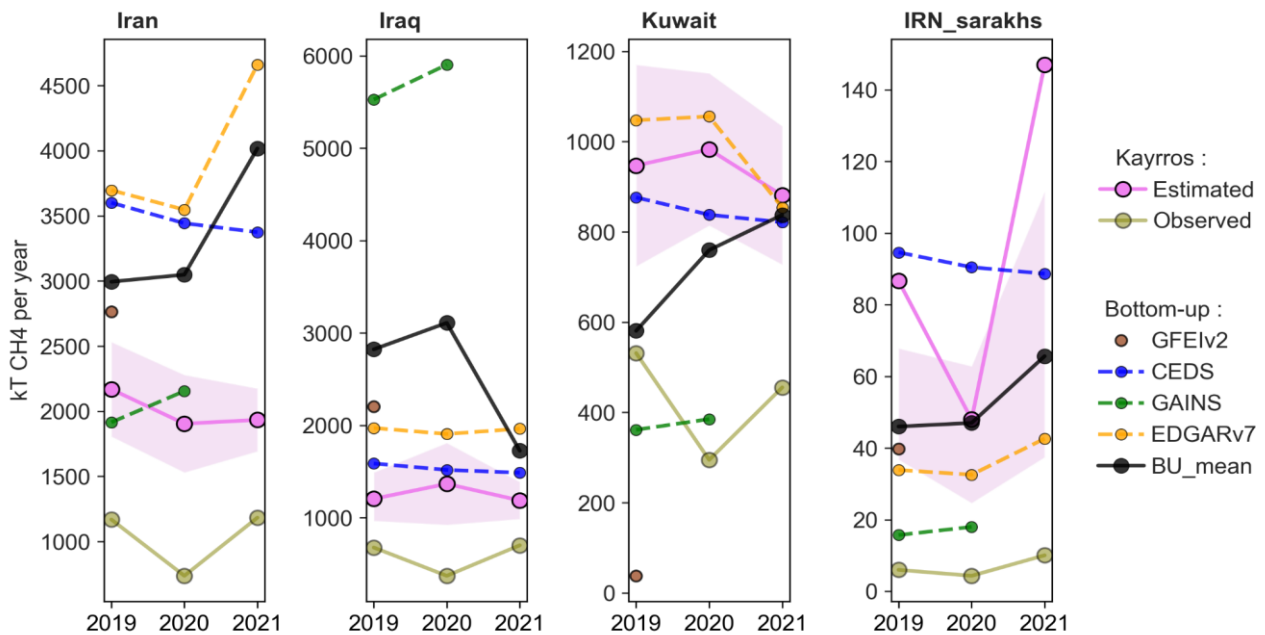


Fig 1.3.3-2. Comparison of methane emissions from major basins in the EMME between regional inversions from Kayrros and bottom-up inventories.

Unlike Iran and Iraq, the mean emissions from bottom-up inventories for Kuwait is ~25% lower than the regional inversions during 2019-2021, with a better agreement in emissions in the year 2021. This discrepancy is mostly driven by emissions from GAINS and GFEv2 which are around 60% and above 90% lower than regional inversions respectively. Emissions from other bottom-up inventories lie within the bounds reported in regional inversions with EDGARv7 5% higher and CEDS ~10% lower than regional inversions. For IRN_sarakhs, the mean emissions from bottom-up inventories show a good agreement with the regional inversions. This is driven by the compensating effects from double emissions in CEDS and ~70% lower emissions in GAINS with EDGARv7 and GFEIv2 showing good agreement.

1.3.4 Atmospheric analysis of NO_x emissions using a global inversion

Atmospheric pollutants and greenhouse gases emit in the atmosphere due to human anthropogenic activities (i.e., use of fossil fuel, demand of energy and industrial progress related to socio-economy growth, transportation, agriculture practice, and waste management, etc.). These pollutants adversely affect the atmosphere, biosphere, and human wellbeing.

NO₂ is one of the major pollutants affecting human health (such as respiratory disease), air quality, biosphere and climate mainly released to the atmosphere due to anthropogenic activity such as power plant, transport, fossil fuel etc. Therefore, it is very important to monitor the day-to-day variability of atmospheric NO₂ and its surface anthropogenic emissions. **The EMME region is one the significant contributor of anthropogenic NO_x emission mainly due to fossil fuel combustion.** Ozone Monitoring Instrument (OMI), TROPOspheric Monitoring Instrument (TROPOMI) are deployed to monitor the atmospheric GHG, and pollutants (i.e., NO₂ etc.).

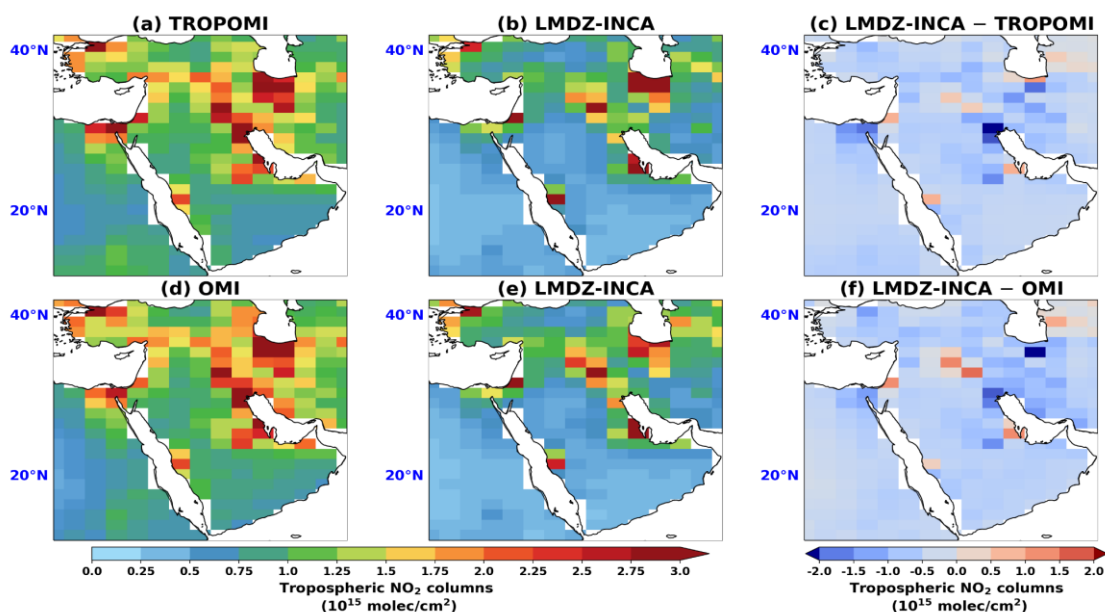
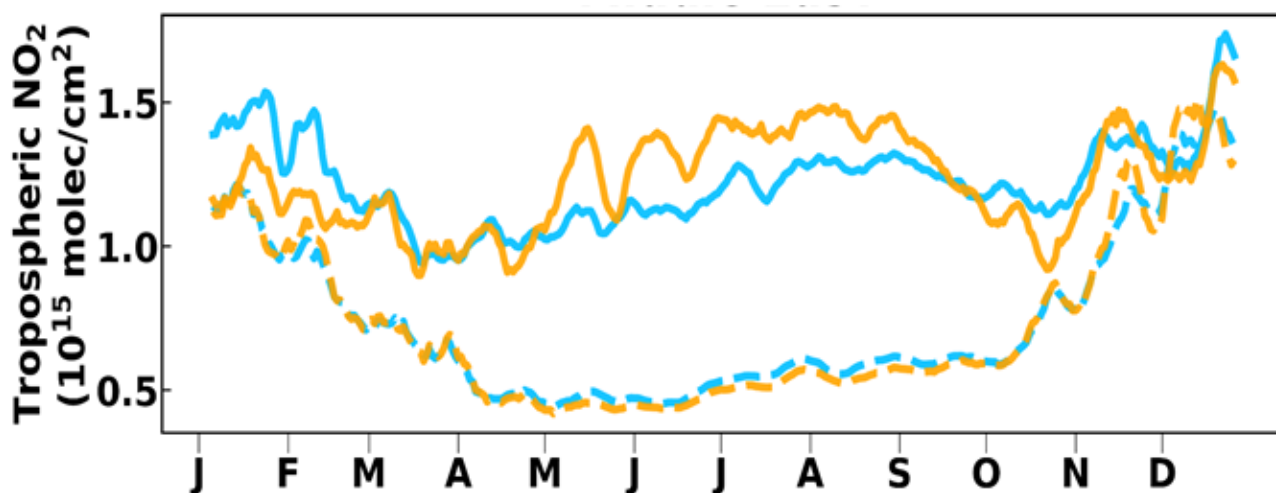


Figure 1.3.4-1: Spatial distribution of annual mean total column NO_2 from TROPOMI, OMI, model simulation by LMDZ-INCA for 2019 with a spatial resolution of 1.27×2.5 over EMME region (a,b,d,e). Annual mean difference between simulated NO_2 and observed NO_2 from TROPOMI and OMI for 2019 with a spatial resolution of 1.27×2.5 over EMME region (c, f).

High NO_2 concentration is observed along gulf of Arabia, Riyadh, Tehran, Cairo, Kuwait City, Baghdad etc from both of the satellite i.e., TROPOMI and OMI during 2019 with a maximum value of $\sim 2 \times 10^{15} \text{ molec/cm}^2$ (**Figure 1.3.4 a and b**). Both the satellite observations are consistent in capturing the annual mean distribution over EMME region during 2019. The model is able to capture the observation with a less magnitude (Figure 1.3.4-1 b and d). The **Figure 1.3.4-1 c and f** describe the model bias i.e., the difference between model simulated and observations atmospheric total column NO_2 . The model exhibits a maximum negative bias with a value of $\sim -2 \times 10^{15} \text{ molec/cm}^2$ over Kuwait city with respect to TROPOMI observation. However, in the case of OMI, the model has a maximum negative bias with a value of $\sim -2 \times 10^{15} \text{ molec/cm}^2$ over Tehran. The model also exhibits negative bias with a magnitude of $\sim -1.5 \times 10^{15} \text{ molec/cm}^2$ over Riyadh with respect to both the observations from TROMO and OMI. A negative bias with a magnitude of $\sim -1.5 \times 10^{15} \text{ molecules/cm}^2$ and $\sim -1.0 \times 10^{15} \text{ molecules/cm}^2$ are noticed over Cairo for TROPOMI and OMI, respectively. Overall, the model bias is observed from ~ 0.5 to $-1.0 \times 10^{15} \text{ molec/cm}^2$ over the EMME region.



— TROPOMI — OMI
- - LMDZ-INCA (TROPOMI) - - LMDZ-INCA (OMI)

Figure 1.3.4-2: Daily mean (10-days running mean) variability of tropospheric column NO₂ for TROPOMI, OMI and LMDZ-INCA during 2019 averaged over the EMME region (unit: 10¹⁵× molec/cm²).

The TROPOMI and OMI showed similar seasonality over the EMME region (**Figure 1.3.4-2**). However, the TROPOMI indicated high (low) tropospheric column NO₂ during January-March (May-September) compared to OMI observation. In case of TROPOMI, we observed high tropospheric column NO₂ during winter (~1.5 10¹⁵× molec/cm²) than summer (~1.2 10¹⁵× molec/cm²). However, in the case of OMI high tropospheric column NO₂ is noticed during summer (~1.4 10¹⁵× molec/cm²) as compared to winter (~1.2 10¹⁵× molec/cm²). The TROPOMI evinced the minimum tropospheric column NO₂ during May-April. However, in the case of OMI, the minimum tropospheric column NO₂ is observed during October-November. The LMDZ-INCA underestimated both of the observations from TROPOMI and OMI during March-October by a factor of ~2. The model and observations exhibit opposite seasonality during June-August.

We inferred the posterior fluxes using a method developed from mass-balanced method as in [Zheng et al. \(2020\)](#) and observation from TROPOMI and OMI during 2019-2021.

Figure 1.3.4-3 describes the annual mean spatial distribution of bottom-up inventory (i.e., CEDS), and estimated fluxes constrained by TROPOMI and OMI. The CEDS and estimated fluxes constrained by TROPOMI and OMI are similar with a magnitude ~ 2 10-10 kg-NO m-2 s-1. The TROPOMI and OMI observations do not show strong reduction of atmospheric NO₂ during 2020 as compared to 2019. Moreover, the observations for both years (i.e., 2020 and 2021) are similar. So, we observed similar estimated fluxes for both years. High NO₂ emission observed from Tehran, Jeddah, Baghdad with a magnitude of ~ 2 10-10 kg-NO m-2 s-1.

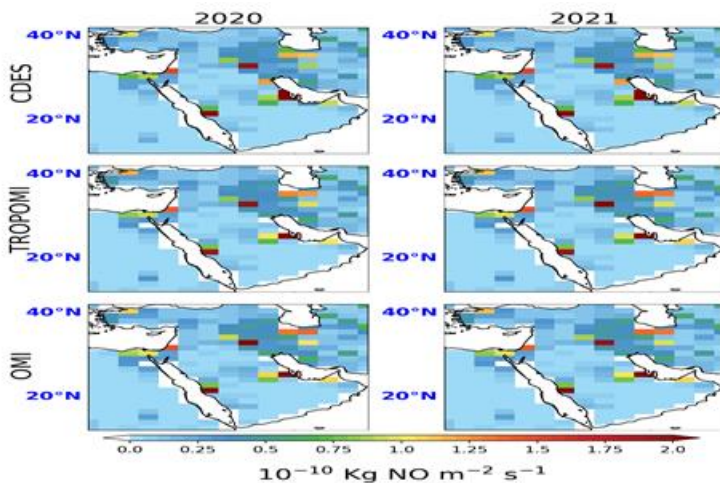


Fig. 1.3.4-3: Spatial distribution of annual mean bottom-up inventory (CEDS), and estimated fluxes constrained by TROPOMI and OMI over EMME region for 2020 and 2021 with a horizontal resolution of 1.27x2.5 (unit: 10-10 kn-NO m-2 s-1).

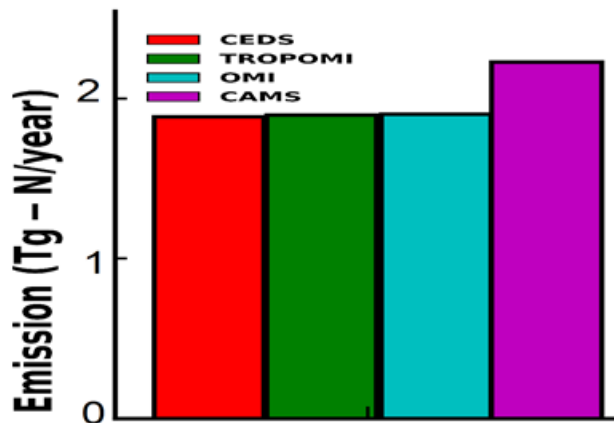


Fig. 1.3.4-4: Annual mean bottom-up inventories (i.e., CEDS), and posterior inversion fluxes constrained by TROPOMI, OMI, and independent inventory (i.e., CAMS) calculated during 2020-2021 over EMME region (unit: Tg-N/year).

Figure 1.3.4-4 shows annual mean bottom-up inventories (i.e., CEDS), and posterior fluxes constrained by TROPOMI, OMI, and independent inventory (i.e., CAMS) calculated during 2020-2021 over EMME region. The mean annual flux of CEDS, and TROPOMI and OMI constrained fluxes are similar with a magnitude of ~ 1.9 Tg-N/year. However, the annual mean CAMS evidenced ~ 2.2 Tg-N/year over the same region during 2020-2021.

1.3.5 Atmospheric analysis of NO_x emissions using a regional inversion

Urban areas and industrial facilities are recognized as prominent sources of nitrogen oxides (NO_x = NO + NO₂) due to their significant concentration of human activities and industrial production. In the Eastern Mediterranean and Middle East (EMME) region, the industrial production and the consumption of fossil fuels, predominantly through road transport and electricity generation, contribute to high NO_x pollution levels that can be monitored from space-based observations. The Tropospheric Monitoring Instrument (TROPOMI) provides daily NO₂ images which enable the detection of plumes with a spatial resolution of up to 3.5x7km². The corresponding product provides a quality insurance for the retrievals that characterise clear-sky conditions (above a certain threshold), which are prevalent in the region due to its desert features. Furthermore, the observed NO₂ plumes exhibit a high signal-to-noise ratio above the primary hotspots within the region, attributable to the short lifetime of NO₂ and the intense anthropogenic activities in sprawling megacities and industrial zones.

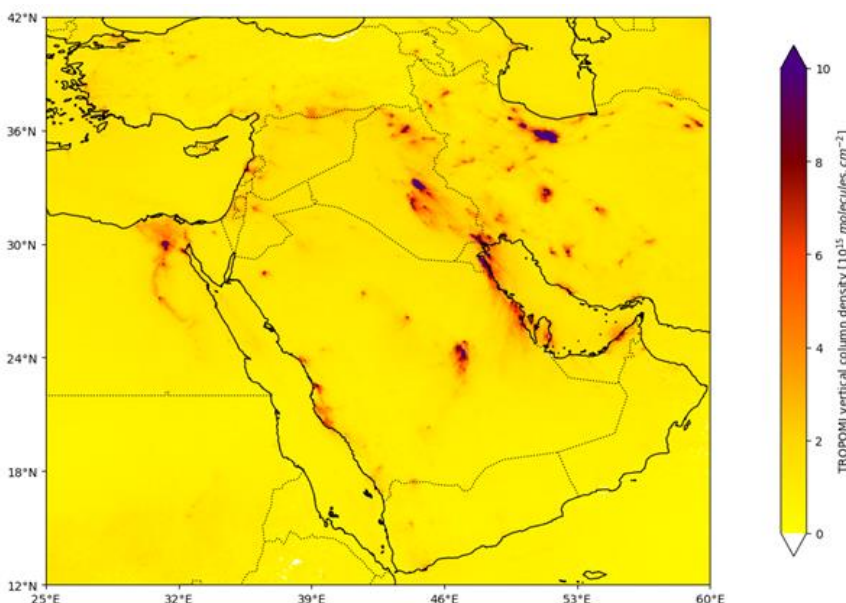


Figure 1.3.5-1: Mean TROPOMI nitrogen dioxide tropospheric vertical column density above the EMME region from 2022/07/01 to 2022/07/14 regridded with a 0.0625°x0.0625° resolution. White pixels correspond to areas for which the quality of TROPOMI measurements were systematically under a quality flag threshold.

To infer NO_x emissions from TROPOMI images, a flux-divergence scheme based on a mass continuity equation (Beirle et al., 2019), expresses NO_x production as the sum of a wind transport term and a chemical sink term representing the reaction between NO₂ and hydroxyl radical (OH). NO₂ production is then scaled up to NO_x emissions using a Leighton ratio. Horizontal wind is taken from ERA5 while other parameters, involved in the calculation of the sink term, are taken from CAMS NRT data. This method facilitates the identification of most NO_x hotspots within the region, as well as the main roads and shipping lanes. This mapping technique can be employed at a more localised scale to infer the emissions of specific countries, such as Egypt and Qatar. Notably, from 2019 to 2022, the average NO_x emissions of Egypt and Qatar amounted to 353 and 115 kilotons (expressed as NO₂) respectively, with weekly cycles that are consistent with the social norms prevalent in these countries. The estimation of NO_x emissions from isolated industrial facilities such as power plants is also feasible: for instance, our estimations indicate daytime emissions of 1.86 tons per hour from the three gas power plants situated in Ras Laffan, Qatar, while in Cyprus, the five distinct power plants on the island have daytime emissions ranging from 0.1 to 0.4 tons per hour. Such estimates have been able to compensate for outdated and incomplete inventories that characterise the two countries.

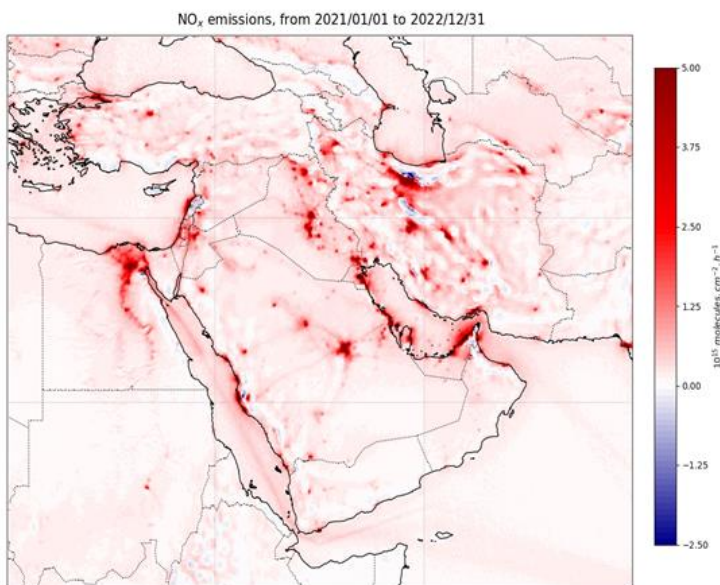


Figure 1.3.5-2: Mean NO_x emissions from 2021 to 2022 on a 0.0625°x0.0625° resolution. Note that the region covers three time zones; this map is therefore asynchronous but represents emissions calculated at around 13:30 local time.

Within the EMME region, our method encounters certain challenges when estimating emissions in areas characterised by complex topography, such as Iran, Türkiye, and Lebanon. Additionally, the resolution of the parameters involved in emissions calculations, particularly horizontal wind (0.25°x0.25°) and OH concentration (0.4°x0.4°), is a significant constraint on the accuracy of our approach. Finally, our method is inherently reliant on the modelling of chemical loss, which necessitates the utilisation of parameters estimated through ECMWF data and is represented by only the two major chemical reactions involved in daytime NO_x chemistry.

We believe that such a method can be reproduced in other regions of the world that share similar characteristics as the EMME region. The development of similar applications is likely to provide better monitoring of global anthropogenic emissions, and compensate for non-existent, inaccurate or outdated inventories by providing low-latency emissions, therefore helping countries to report their emissions of air pollutants.

1.3.6 Atmospheric analysis of SO₂ emissions using a global inversion

SO₂ is released into the Earth's atmosphere through natural and anthropogenic processes and the latter category amounts to the majority of the global SO₂ emissions. While the global anthropogenic SO₂ emissions has shown a decline trend over the past decade, **the EMME region remains one of the major hotspots of the anthropogenic SO₂ emissions on the Earth with their relative contribution increased from ~13% in 2005 to ~24% in 2020** (Fioletov et al., 2023). The anthropogenic SO₂ emissions in the EMME region primarily originate from the power plants involved in fossil energy production and oil- and gas-related sources such as oil refineries. A recent study (Fioletov et al., 2023) based on the point source emissions derived from the satellite observations showed an increase in the number of these sources in this region. Ground-based air-quality measurements in the EMME region are limited (Ukhov, et al., 2020). However, satellite SO₂ observations have been used to monitor SO₂ emissions at different regional and global scales and to detect large point sources of SO₂ emissions of diverse origins (Koukoulis et al., 2018, Qu et al., 2019; Fioletov et al., 2023). Inversion methods by combining the satellite observations with atmospheric transport models can infer the spatial distribution and intensity of anthropogenic SO₂ emissions. In this study, we performed global inversions of SO₂ anthropogenic emissions using TROPOMI SO₂ vertical column density (VCD) observations and a global chemistry transport model LMDZ-INCA over three years from 2019 to 2021. The emission estimates from the global SO₂ inversions are analysed over the EMME region.

We used the global chemistry coupled transport model LMDZ-INCA with 1.26° × 2.5° (latitude × longitude) horizontal resolution and 79 hybrid σ -p vertical levels extending up to the stratosphere (Hauglustaine et al., 2004). The model uses a priori monthly global anthropogenic emission inventories from the open-source Community Emissions Data System (CEDS) (McDuffie et al., 2020). The global LMDZ-INCA simulations consist in a spin-up from 2010 to 2018 and then on simulations from 2019, which are evaluated with the satellite observations. As the TROPOMI operational offline L2 SO₂ data product has high noise levels, we used the TROPOMI COBRA SO₂ data product (Theys et al., 2021) in this study which has comparatively smaller noise. Since we aim to optimise only the anthropogenic SO₂ emissions, we minimise the contributions of transported volcanic plumes by manually tracking the volcanic SO₂ plumes transported from explosive volcanoes to the EMME region and filtered out the corresponding TROPOMI pixels from analysis and inversions. We used an inversion method described in Zheng et al. (2020) to estimate the daily SO₂ anthropogenic fluxes. The inversion derives the fluxes using daily averaged (as 10-day running mean) simulated and observed VCDs, the local sensitivity of VCDs to emission changes with 40% reduced anthropogenic SO₂ emission for a reference year 2019, and the year-to-year observation changes of a year of interest (e.g., for 2020 or 2021) compared to the observations of year 2019.

Figure 1.3.6-1 shows an example of the annual averaged simulated SO₂ VCDs from LMDZ-INCA compared with the TROPOMI-COBRA observations over the EMME region for the year 2019. TROPOMI SO₂ observations in this figure clearly show **high values of SO₂ VCDs over the United Arab Emirates, Qatar, Bahrain, Kuwait, Iraq, Iran, Turkey, Saudi Arabia**, etc. It also indicates that LMDZ-INCA overestimates SO₂ VCDs in comparison to the observed TROPOMI VCDs over the polluted areas in the EMME regions. The TROPOMI SO₂ VCDs averaged over the EMME regions during DJF and SON seasons (~0.10 DU) are higher compared to MAM and JJA seasons (~0.07 DU). In all seasons except for DJF, where the modelled averaged VCDs (~0.12 DU) are comparable with the TROPOMI observations (~0.10 DU), the model overestimates by at least a factor of two.

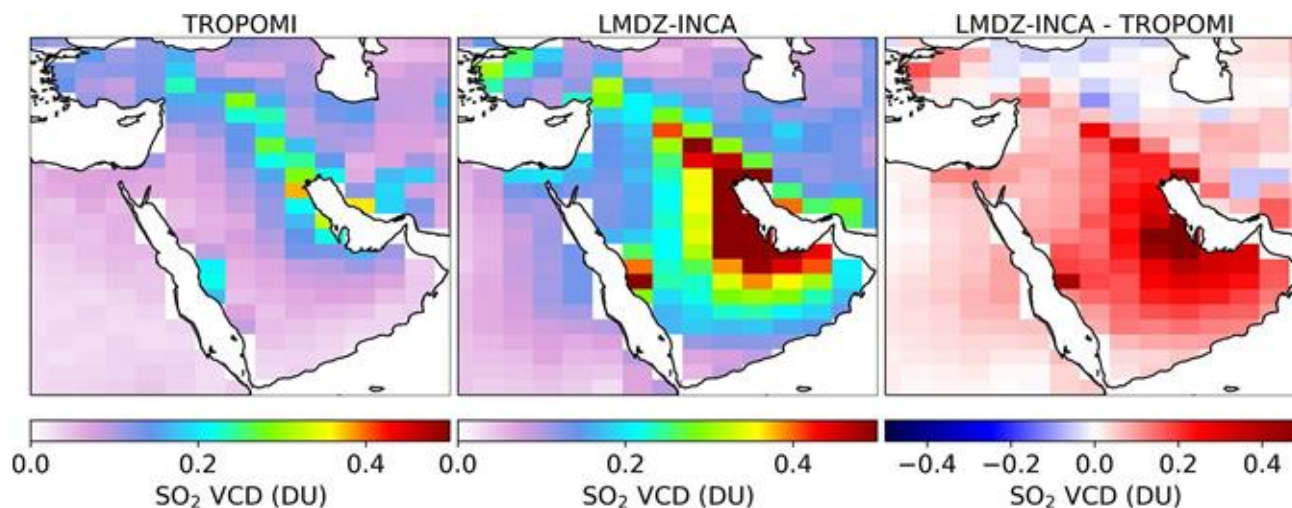


Figure 1.3.6-1: Annual averages of the SO₂ vertical column density (VCD) observed by TROPOMI (left) projected on the LMDZ-INCA model grids, simulated by LMDZ-INCA (middle), and the difference between the model and TROPOMI VCDs (right) for the year 2019.

Figure 1.3.6-2 shows the daily variation of the prior (2019) and the estimated anthropogenic SO₂ emissions of the EMME region constrained by the TROPOMI observations for 2020 and 2021. The trend of the both years' TROPOMI constrained fluxes are almost similar to each other. TROPOMI constrained annual emissions for 2021 is slightly smaller than 2020 with relative difference of ~5%. We also compared the annual TROPOMI constrained emissions aggregated from the daily estimates with the annual CAMS bottom-up anthropogenic SO₂ emissions aggregated from monthly values sub-sampled on the common grids (1.27°×2.5°) of the estimated emission for 2020 and 2021 (**Figure 1.9-2**). TROPOMI constrained annual EMME anthropogenic SO₂ emissions are ~21% and ~47% higher for 2020 (~14% and ~41% for 2021) compared to the CEDS and CAMS emissions, respectively (**Figure 1.9-2**).

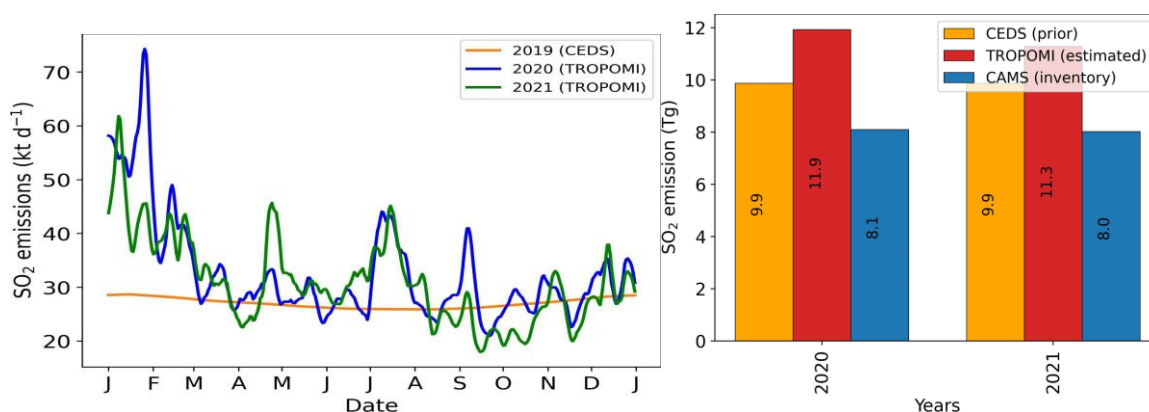


Figure 1.3.6-2: The daily variation of the global anthropogenic SO₂ emissions (sub-sampled on the common grids) for 2020 and 2021 over the EMME region estimated using TROPOMI observations and a priori CEDS bottom-up emissions for 2019 (left) and a comparison of the annual estimated anthropogenic SO₂ emissions with CEDS (prior) and CAMS bottom-up inventories (right).

1.3.7 Atmospheric analysis of NH₃ emissions using a global inversion

Ammonia (NH₃) in the Earth's atmosphere originate from both natural and anthropogenic sources and the anthropogenic emissions dominate over the emissions from the natural one. Agriculture contributes to more than 81% of the total global NH₃ emissions (van Damme et al., 2021) and other sources of the anthropogenic NH₃ emissions mainly stem from domestic, and industrial activities (Sutton et al., 2013). A recent study by Osipov et al. (2022) based on ship-borne measurements from around the Arabian Peninsula and modelling showed that **NH₃ emissions in the Middle East region are significantly underestimated, potentially by a factor exceeding 15**. While natural sources of ammonia play a negligible role in the region, the vast majority of emissions arise from industrial and agricultural activities. Osipov et al. (2022) also highlighted that the satellite derived point sources alone, e.g. from van Damme et al. (2018), are inadequate for a realistic NH₃ background in this region and area sources primarily from agriculture sources have a significant impact in this regard. Thus, the uncertainty in the anthropogenic NH₃ emissions for the EMME region is notably high. In this study, we used NH₃ VCD observations from the IASI V3R.1.0 NH₃ data product for the global inversions of anthropogenic NH₃ emissions and the estimated fluxes over the EMME region are analysed in detail. We select only land measurements from the morning overpass as IASI is more sensitive at this time to the boundary layer, owing to more favourable thermal conditions. We use the observations only with cloud coverage lower than 10 %. We used the same inversion approach to estimate daily global anthropogenic NH₃ as used for the global inversions of NO_x and SO₂.

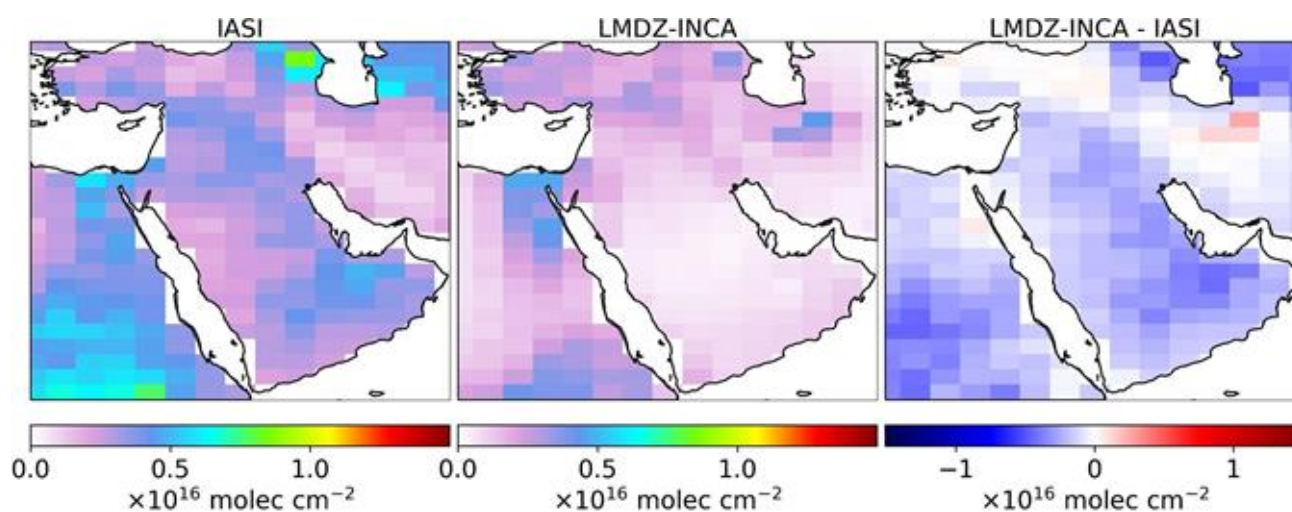


Figure 1.3.7-1: Annual averages of the NH₃ vertical column density (VCD) observed by IASI (left) projected on the LMDZ-INCA model grids, simulated by LMDZ-INCA (middle), and the difference between the model and IASI VCDs (right) for the year 2019.

Figure 1.3.7-1 compares the annual averaged simulated LMDZ-INCA NH₃ VCDs with the IASI observations projected on the model grids over the EMME region. The IASI observations clearly identify the sources of NH₃ emissions over the EMME region, which is largely absent in the LMDZ-INCA simulations. The model underestimates the NH₃ columns compared to the IASI NH₃ observations over most of the EMME region (**Figure 1.10-1**).

Figure 1.3.7-2 shows the daily variation of the IASI constrained anthropogenic NH₃ emissions for 2020 and 2021 and the a priori emissions for 2019 used in the inversions. The estimated anthropogenic NH₃ emissions for both inversion years 2020 and 2021 exhibit a similar trend, with notable high emissions in May, July, and September compared to other months. Annual anthropogenic NH₃ emission of the EMME region in 2021 (3 Tg) is slightly smaller compared to the annual emission of 2.7 Tg in 2020, resulting in a relative difference of ~7%. These annual estimated emissions aggregated from the daily

estimates are compared with the global anthropogenic NH₃ emissions from CEDS and CAMS bottom-up inventories sub-sampled on the common grids over the EMME region (Figure 1.10-2). The estimated annual EMME anthropogenic NH₃ emissions for 2020 and 2021 are ~19% and ~11% higher, respectively, compared to the CEDS emissions. Additionally, compared to the CAMS NH₃ emissions, they are ~42% and ~32% higher, respectively.

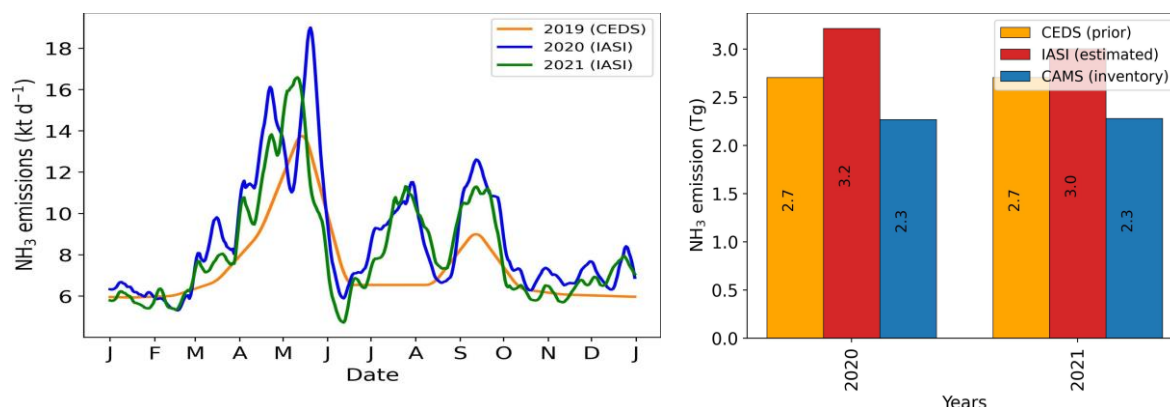


Figure 1.3.7-2: The daily variation of the global anthropogenic NH₃ emissions (sub-sampled on the common grids) for 2020 and 2021 over the EMME region estimated using IASI observations and a priori CEDS bottom-up emissions for 2019 (left) and a comparison of the annual estimated anthropogenic NH₃ emissions with CEDS (prior) and CAMS bottom-up inventories (right).

It is noted that the simple inversion approach for the estimations of the global anthropogenic NO_x, SO₂, and NH₃ emissions fits the relative changes and does not solve for discrepancies between simulation and observations at the given location and time. As such, it strongly relies on the prior emission for the reference year, and in particular on its ability to capture the major spatial and seasonal variations during that year. This seems to raise issues, particularly over the EMME and Indian regions. We need to investigate a hybrid approach that would involve correcting the a priori emissions of the reference year first, and then utilising these corrected a priori emissions in the inversions.

1.4. Establishment of an emission analysis system at Cyl, based on ground-based and satellite data and first applications in atmospheric modelling

1.4.1 Establishment of an emission analysis system at Cyl, based on ground-based and satellite data

Cyprus is a European country that is centrally located in the Eastern Mediterranean Middle East (EMME) region, at the crossroads of natural and anthropogenic pollution from mid- and long- range sources, with pronounced contribution from transported pollution towards the region and large effect of natural sources in the low air quality status. Emission sources from activities performed in the area of interest are not well captured in the regional emission inventories and dedicated effort has been performed to improve the spatiotemporal distribution of emissions as one of the most important components of model skill.

Cyprus is one of the countries in the EMME region that faces challenges with the exceedance of air quality limits and compliance with European regulatory standards. For the year 2017, Cyprus reported the second highest mean annual NO₂ concentrations (13.7 µg/m³) among 41 European countries (European Environment Agency, 2019). The exposure in high NO₂ concentrations in Cyprus is

estimated to cause about 240 premature deaths per year. This translates to 0.02% of the population which is among the highest between the 41 European countries (European Environment Agency, 2019). In addition, exposure to PM_{2.5} is responsible for 473 years of life lost (YLL) per 100,000 inhabitants in Cyprus (European Environment Agency, 2019).

In this task (6.3.c) we assessed the **emission sources over the island of Cyprus and their sectoral contribution**, utilising ground-based and satellite data, and we performed an atmospheric modelling application highlighting the importance of accurate emissions information at local and regional scale.

1.4.2. Inventory Source Comparison

A comparison of the inventory sources considered for Cyprus follows in **Table 1.4.1**. for the years 2000-2021. The nationally reported data published in the Informative Inventory Report of Cyprus for air pollutants may be regarded as the official source of truth. Other emission inventories compiled for gridded use, such as the EDGAR inventories, may consider the officially reported emissions, but also include other external factors.

Due to the incremental nature of updates to the emission inventory reported by Cyprus annually, recalculations may be applied to the entire time series following a change in emission estimation methods. However, these recalculations are not immediately reflected in the EDGAR inventories until the following version, becoming the largest contributing factor when comparing values between the two inventories.

Another distinction arises depending on how the emissions are spatially distributed, and some sectors like Shipping and Aviation may contribute more to this effect than others, especially in islands like Cyprus. The version of EDGAR labelled "Reported" refers to the total emissions attributed to the emitter country, whereas the values labelled "Derived" only include emissions inside the country borders and do not capture transboundary emission sources.

Year	Source	CO (kt)	NH ₃ (kt)	NM VOC (kt)	NO _x (kt)	PM ₁₀ (kt)	PM _{2.5} (kt)	SO ₂ (kt)
2000	EDGAR-v6.1 Derived	51.6	6.0	14.3	22.5	3.0	1.9	20.3
	EDGAR-v6.1 Reported	62.2	7.0	17.5	30.6	3.8	2.3	38.3
	Nationally Reported	29.7	6.6	13.4	22.5	4.5	2.5	47.6
2001	EDGAR-v6.1 Derived	50.4	6.4	14.2	21.9	3.1	2.0	19.0
	EDGAR-v6.1 Reported	60.3	7.4	17.3	29.9	3.8	2.4	36.0
	Nationally Reported	28.4	7.0	13.1	22.5	4.1	2.2	45.3
2002	EDGAR-v6.1 Derived	47.6	6.9	13.8	21.6	3.1	2.0	19.2
	EDGAR-v6.1 Reported	57.0	7.9	16.8	29.6	3.9	2.4	36.2
	Nationally Reported	26.8	7.4	13.8	22.2	4.0	2.1	45.4
2003	EDGAR-v6.1 Derived	47.8	6.9	13.8	22.7	3.3	2.1	20.8
	EDGAR-v6.1 Reported	57.2	7.9	16.9	32.0	4.1	2.5	39.9

	Nationally Reported	26.2	7.2	14.7	22.5	4.0	2.1	47.0
2004	EDGAR-v6.1 Derived	46.6	6.7	13.2	22.5	3.2	2.0	19.7
	EDGAR-v6.1 Reported	55.9	7.7	16.1	31.2	3.9	2.4	37.4
	Nationally Reported	25.0	7.1	15.0	22.3	4.0	2.1	40.3
2005	EDGAR-v6.1 Derived	44.4	6.2	12.6	21.5	3.0	1.8	17.4
	EDGAR-v6.1 Reported	53.3	7.1	15.5	29.8	3.7	2.2	34.4
	Nationally Reported	23.7	6.7	15.6	22.1	3.9	2.1	37.8
2006	EDGAR-v6.1 Derived	41.8	6.6	11.5	20.6	2.9	1.7	16.7
	EDGAR-v6.1 Reported	50.2	7.5	14.1	28.5	3.5	2.1	33.0
	Nationally Reported	21.6	6.8	15.3	21.7	3.7	2.0	31.3
2007	EDGAR-v6.1 Derived	41.3	6.4	11.7	22.2	3.1	1.8	19.1
	EDGAR-v6.1 Reported	49.6	7.3	14.3	28.8	3.8	2.2	32.8
	Nationally Reported	18.1	6.7	15.5	21.2	3.6	1.9	29.2
2008	EDGAR-v6.1 Derived	37.6	6.4	11.2	21.6	3.0	1.8	18.7
	EDGAR-v6.1 Reported	45.3	7.3	13.7	28.1	3.7	2.1	32.1
	Nationally Reported	15.8	6.5	14.2	19.8	3.6	1.8	22.2
2009	EDGAR-v6.1 Derived	33.8	6.2	10.4	20.1	2.7	1.6	17.0
	EDGAR-v6.1 Reported	40.6	7.2	12.6	25.9	3.3	2.0	29.3
	Nationally Reported	14.4	6.4	13.0	20.0	3.1	1.6	17.6
2010	EDGAR-v6.1 Derived	30.4	6.0	10.0	19.3	2.5	1.6	15.4
	EDGAR-v6.1 Reported	36.4	6.9	12.2	24.5	3.0	1.9	26.6
	HTAP-v2 Monthly	15.2	4.7	6.9	16.7	3.8	2.0	14.9
	Nationally Reported	13.8	6.3	12.7	18.6	3.0	1.5	21.8
2011	EDGAR-v6.1 Derived	26.8	5.9	9.6	18.1	2.2	1.4	14.8
	EDGAR-v6.1 Reported	32.1	6.8	11.7	22.9	2.7	1.6	25.6
	Nationally Reported	12.7	6.2	8.8	21.4	2.7	1.4	20.8
2012	EDGAR-v6.1 Derived	23.1	5.7	9.0	16.4	2.0	1.2	13.6
	EDGAR-v6.1 Reported	27.5	6.6	11.0	20.0	2.5	1.4	22.9
	Nationally Reported	12.5	5.9	8.5	20.8	2.0	1.1	16.1
2013	EDGAR-v6.1 Derived	19.1	5.0	8.2	14.3	1.8	1.1	11.6

	EDGAR-v6.1 Reported	22.7	5.8	9.9	16.4	2.2	1.3	18.9
	Nationally Reported	11.5	5.5	7.4	15.3	1.7	0.9	13.5
2014	EDGAR-v6.1 Derived	17.2	5.4	8.8	14.7	1.9	1.2	12.6
	EDGAR-v6.1 Reported	20.5	6.2	10.9	17.0	2.3	1.4	20.3
	Nationally Reported	11.8	5.8	7.2	16.0	1.5	0.9	16.7
2015	EDGAR-v5 Monthly	19.2	5.5	8.7	14.7	2.1	1.3	12.5
	EDGAR-v6.1 Derived	18.7	5.3	9.1	15.4	2.1	1.3	12.8
	EDGAR-v6.1 Reported	22.1	6.2	11.0	17.5	2.5	1.5	20.7
	Nationally Reported	11.3	5.0	7.0	13.7	1.6	0.9	12.8
2016	EDGAR-v6.1 Derived	17.6	5.4	9.3	15.8	2.1	1.3	13.5
	EDGAR-v6.1 Reported	21.1	6.2	11.4	18.5	2.6	1.5	22.2
	Nationally Reported	11.7	5.2	8.1	13.6	1.7	1.0	16.1
2017	EDGAR-v6.1 Derived	19.2	5.5	9.8	16.6	2.5	1.5	13.7
	EDGAR-v6.1 Reported	22.8	6.3	12.0	18.8	3.0	1.7	22.2
	Nationally Reported	11.6	5.2	8.6	13.5	1.8	1.0	16.3
2018	EDGAR-v6.1 Derived	19.8	5.7	10.1	17.0	2.6	1.6	13.9
	EDGAR-v6.1 Monthly	20.9	5.7	10.5	17.0	2.7	1.6	13.9
	EDGAR-v6.1 Reported	23.4	6.5	12.3	18.9	3.1	1.8	22.2
	Nationally Reported	11.0	5.4	7.8	13.1	1.8	1.0	16.9
2019	Nationally Reported	10.9	5.5	7.6	14.3	2.0	1.0	15.9
2020	Nationally Reported	9.7	5.7	7.4	11.6	1.8	0.9	11.6
2021	Nationally Reported	10.3	5.9	7.7	12.2	1.9	1.0	9.9

Table 1.4-1. Inventory sources considered for Cyprus for the years 2000-2021

Despite the variations and uncertainties in these emission inventories there is a clear decreasing trend in the fluxes of all the primary pollutants included in this process (**Fig. 1.4-1**). The lowest values are observed in the 2012-2013 period, that was a period of economic recession for the country, followed by a slightly increasing rate in the subsequent years. In the regional and global inventory databases (mainly green and orange lines), national emissions for all species in Cyprus seem to be steadily decreasing and pertain to the low rates until 2014, with a trend reversal in the recent years, still, however remaining below the average values of the decade 2000-2010. The remission rate is captured to be slower in the national inventory databases (blue lines) or not captured at all.

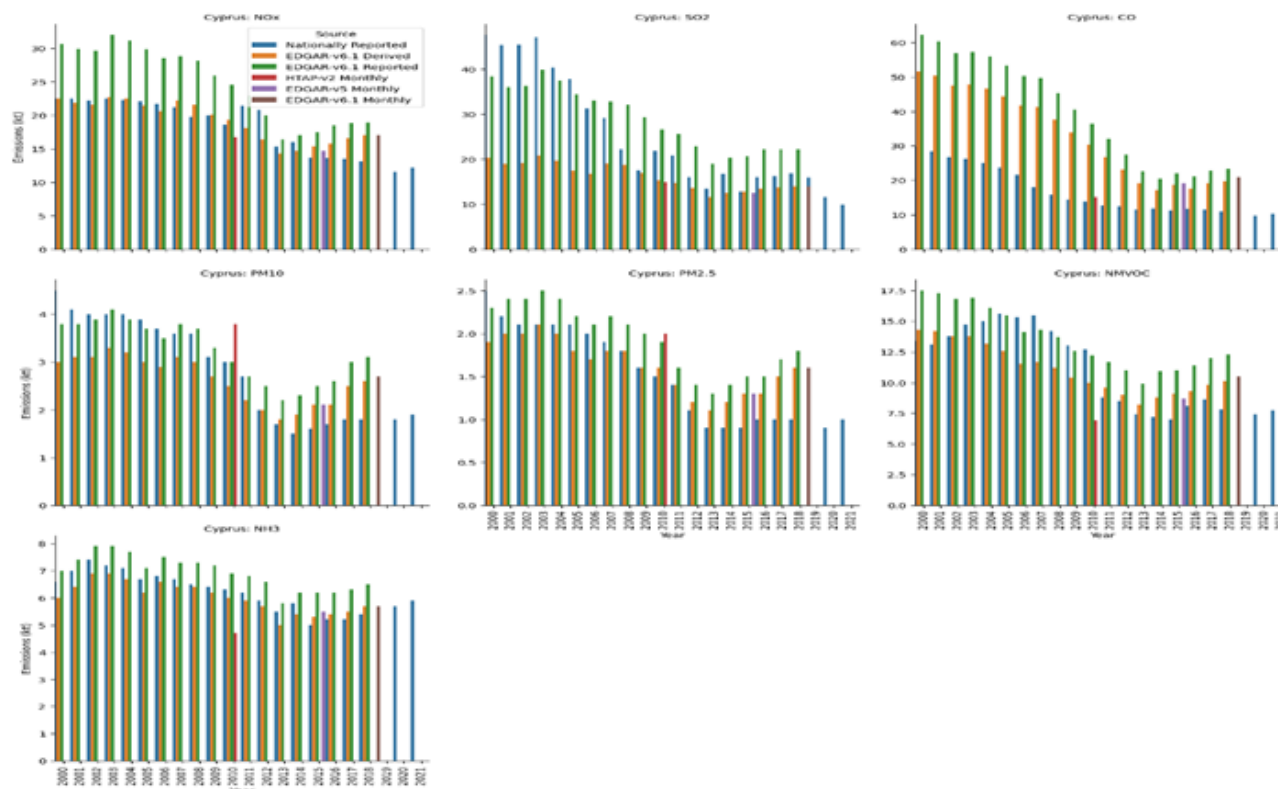


Fig.1.4-1. Time series of total national emissions per species from nationally reported estimates and global annual and monthly emission databases from 2000 until 2021

1.4.3. Sectoral Emission Analysis

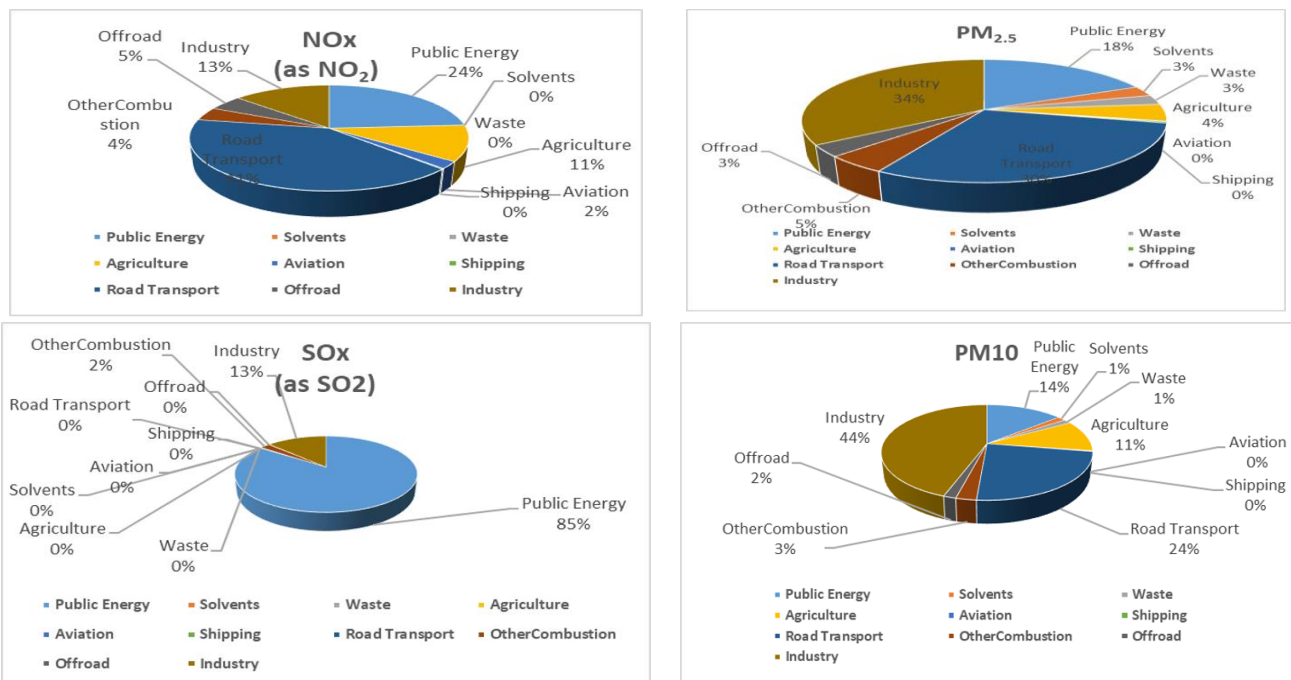
Emissions from **road transport dominate the NO_x emissions (41%)** while there is also an important contribution from **energy production (24%)**, followed by **industrial processes (13%)** and agriculture. Industrial processes and road transport are also the main local source of particulate matter, followed by energy production (18% for fine aerosols and 14% for coarser species) and also agriculture for large aerosol mixtures (11%). Black carbon (BC), also known as soot, is another aerosol species emitted from anthropogenic activities and important for air quality modelling applications, thus included in gridded emission inventories used in such studies. At national level **road transport has the highest contribution to the levels of BC (55%)** followed by industrial activities (26%).

Gaseous species emitted from human related activities also include **SO₂ for which public energy production and use plays an important role (85%)** and to a lesser extent industry (13%), **carbon monoxide dominated by road transport and industry (63% and 25%)**, and non-methane volatile organic compounds that are mostly emitted by solvents, agriculture and road transport (33%, 27% and 25% respectively).

Throughout the last 30 years, the **Cyprus NO_x emissions (NO and NO₂) decreased by 5.89 Gg in the 1990 – 2021 period**, corresponding to 32% of the national total in 1990 and decreased by 9.81 Gg in the 2005 – 2020 period, corresponding to 44% of the national total in 2005. The main contributors are the road transport emissions, the public power generation and the industry sectors. The emissions due to the industry sector remain almost constant throughout the years. Regarding the emissions from the road transport sector, the emissions per vehicle decreased significantly during the period 1990 – 2019 due to the implementation of new car technologies and the usage of better-quality fuels, but were, somehow, counterbalanced by an increase in the number of vehicles and mileage per year per vehicle.

The PM₁₀ emissions decreased by 2.67 Gg in the 2000 – 2021 period, corresponding to 59% of the national total in 2000. The main contributors to this decrease are public power generation, the road transport and the industry. The PM_{2.5} emissions decreased by 1.48 Gg in the 2000 – 2021 period, corresponding to 64% of the national total in 2000 and decreased by 1.09 Gg in the 2005 – 2021 period. Throughout the last years, the Cyprus SO_x emissions (SO₂) decreased by 22.01 Gg in the 1990 – 2021 period, corresponding to 69% of the national total in 1990 and decreased by 27.93 Gg in the 2005 – 2021 period. The main contributors to this decrease are the power generation sector, as well as the industry, other stationary combustion and road transport sectors. The sulphur content in fuels consumed by those sectors was reduced. This is mainly due to the transposition and enforcement of the relevant EU Directives regarding the sulphur content in the fuels. Currently, the energy sector is responsible for 88% of the national SO_x emissions. The Cyprus CO emissions decreased by 34.53 Gg in the 1990 – 2021 period, corresponding to 77% of the national total in 1990 and decreased by 13.40 Gg in the 2005 – 2021 period, corresponding to 57% of the national total in 2005. The main contributor to this decrease is the road transport sector and the improvement of car technologies. Currently, the road transport sector is responsible for about 63% of the national CO emissions in 2021. The Cyprus NMVOC emissions decreased by 5.66 Gg in the 1990 – 2021 period, corresponding to 42% of the national total in 1990 and decreased by 7.90 Gg in the 2005 – 2020 period, corresponding to 51% of the national total in 2005.

Detailed information on the contribution of each sector to the national totals of the emissions of each pollutant are summarised in the pie charts of **Fig. 1.4-2**.



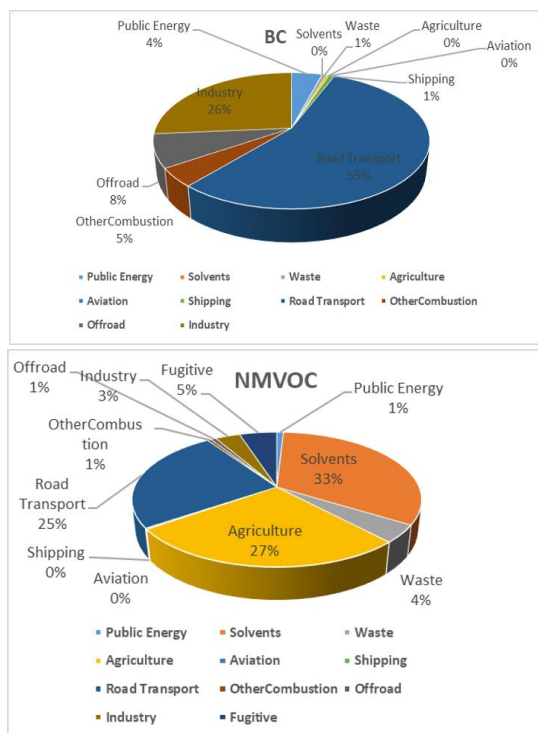


Fig.1.4-2. Distribution of national total emissions per sector and per pollutant

1.4.4. Gridded emission information modelling applications

The performance of air quality models is strongly associated with the quality of their input data. In particular, pollutant emission fluxes are found to be a determining factor regarding the ability of a model to successfully simulate the concentrations of atmospheric constituents. The low spatial resolution of emission inventories is reported as the main reason behind differences between modelled and observed concentrations in high-resolution applications. The incorporation of daily, weekly, and monthly variation in the emission inventory has also been found to lead to better agreement between the model output and observations, especially over industrial and urban areas. The ability of a model to successfully simulate the concentrations of atmospheric pollutants at the urban locations is of great importance for exposure assessment since the majority of the human population lives in these areas, especially in the EMME. Thus, modelling studies that address the impacts of air pollution on human health and the implementation of mitigation strategies often focus on the urban areas.

A new, high-resolution (1x1 km²) emission inventory (henceforth termed HiRes) has been implemented in the area controlled by the Republic of Cyprus, using up-to-date and finer resolution emission data provided by the Cyprus Department of Labour Inspection (DLI), in order to achieve a more accurate representation of the local anthropogenic emissions. Specifically, the total reported emissions of CO, NO_x, NMVOC, SO₂, and PM for the year 2013 on a 1 kmx1 km resolution were re-gridded using a nearest-neighbour grid-point attribution algorithm. The temporal variation of the emission inventory in the model is scaled to include hourly intra- and inter-day (day-of-the-week and month-of-the-year) variations of anthropogenic emissions.

Fig. 1.4-3 shows the annual average anthropogenic emission fluxes of CO, NO_x, NMVOC, and PM_{2.5} in the JRC EDGAR (left) and HiRes (right) emission inventories. The HiRes emission inventory resolves more accurately human activities in terms of spatial distribution since the highly populated areas and the main transport roads are distinguished. The monthly average emissions of CO, NO_x, and PM_{2.5} for winter and summer are shown in **Fig. 1.4-4** for the EDGAR and HiRes emission inventories. The EDGAR inventory provides similar CO emissions for winter and summer (~ 1500x10³kg/mo). The

corresponding values from the HiRes emission inventory are markedly higher, at 3900×10^3 kg/mo during winter and 2850×10^3 kg/mo during summer.

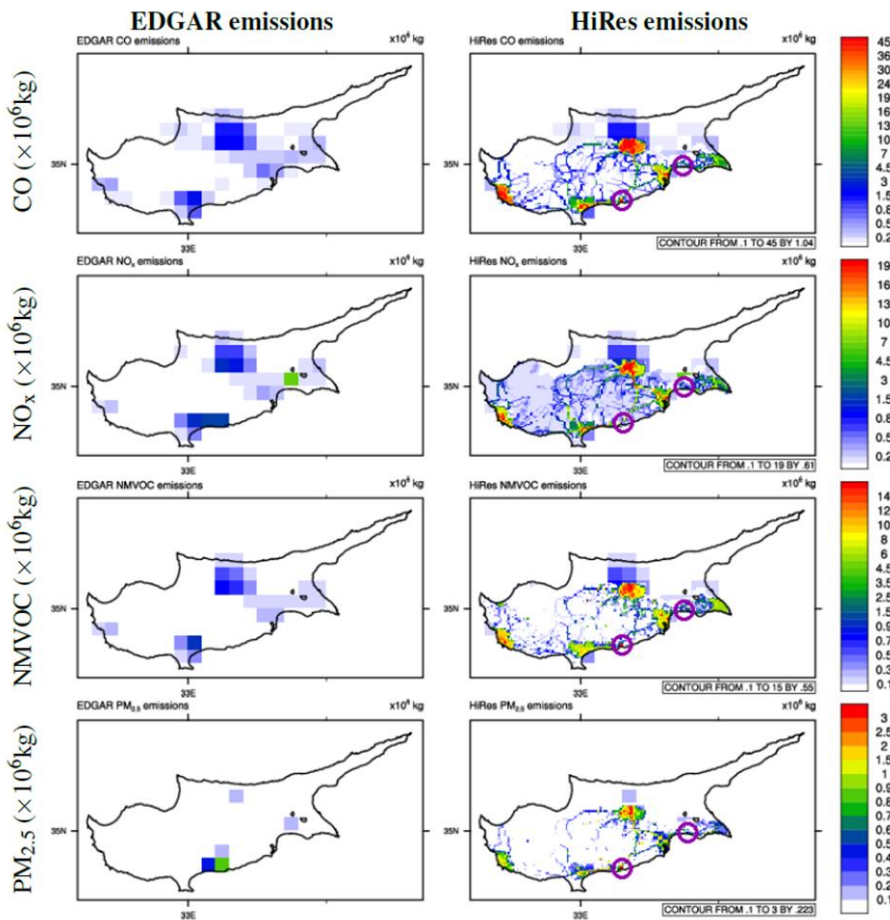


Fig. 1.4- 3: Total annual anthropogenic emissions of CO (a), NO_x (b), NMVOC (c), and PM_{2.5} (d) from the EDGAR (left) and HiRes (right) emission inventories. The magenta circles indicate the locations of the two power stations.

Similarly, NO_x emissions from the EDGAR emission inventory do not significantly differ between winter (1640×10^3 kg/mo) and summer (1430×10^3 kg/mo), whereas winter and summer NO_x emissions from the HiRes emission inventory differ at 3200×10^3 kg/mo and 2350×10^3 kg/mo respectively, representing almost double values compared to EDGAR.

Contrary to the CO and NO_x emissions, PM_{2.5} emissions do not significantly differ between the two inventories. During summer, PM_{2.5} emissions from both inventories reach up to 0.05×10^3 kg/mo. Emissions from the HiRes emission inventory remain the same during winter, while they are slightly increased (0.06×10^3 kg/mo) for the EDGAR inventory. Although the two emission inventories yield similar PM_{2.5} emissions, there are large differences in the spatial distribution, with the emissions from the EDGAR inventory concentrated in the locations of the two power generation stations and the city of Nicosia, and emissions from the HiRes emission inventory distributed to all locations with anthropogenic activity.

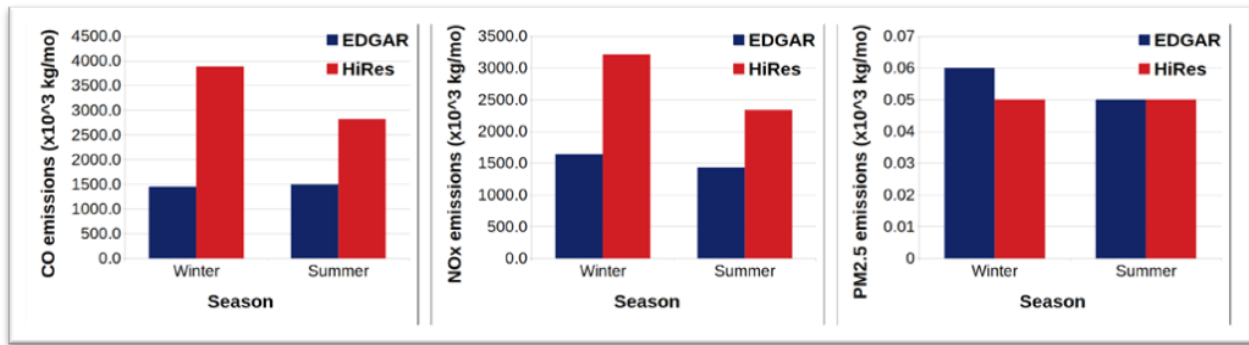


Fig. 1.4-4: Average monthly emissions for CO (left), NOx (centre), and PM2.5 (right) from the EDGAR (blue) and HiRes (red) emission inventories over Cyprus.

Based on LOTOS-EUROS, monthly, weekly, and diurnal emission cycles are applied to each species according to the predominant emission activity per season, as derived from national emission reports. The emission factors for power generation are applied for all species at the locations of the two operational power stations in Cyprus (**Fig. 1.4-4**, magenta circles). In these locations, which are represented by a single grid cell, emissions are much higher compared to the rest of the island. The emission factors applied to the power station locations are shown in **Fig. 1.4-5**.

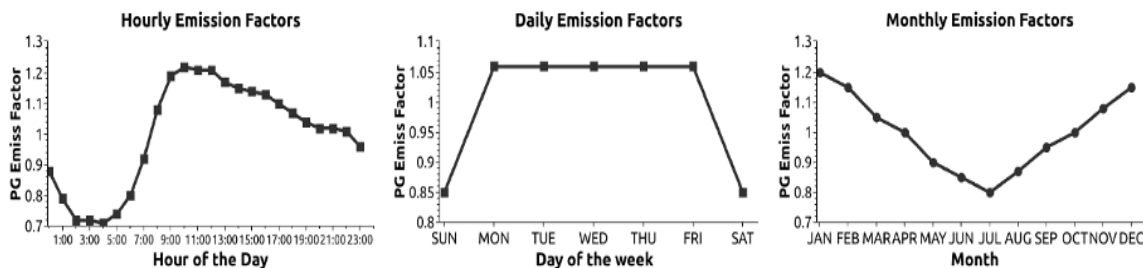


Fig. 1.4-5: Hour of the day (left), day of the week (centre), and month of the year (right) emission factors for power generation.

The hourly, daily, and monthly emission factors applied to each species for all other locations on the island are shown in **Fig. 1.4.6**. Wintertime CO and NOx emissions are dominated by residential combustion whereas during summer traffic consists the main source of emissions. During the day, the emission profile of CO and NOx yields two maxima during both seasons. The first one appears during the morning hours (09:00 LST) whilst the second one appears around 20:00 LST during winter affected mainly by energy consumption for heating and 18:00 LST during summer driven by increased traffic activity. Daily emission factors are constant during weekdays in winter and they slightly increase during summer with a maximum on Friday. An important reduction though is shown during the weekend for both seasons. CO and NOx emissions are considerably higher during the winter compared to the summer.

PM and SO₂ emissions are dominated by industrial processes during both seasons. Thus, a constant emission factor is applied during the day. Regarding the day-to-day variation, emissions of PM and SO₂ are constant during the week, with an abrupt decrease during the weekend due to the reduced industrial activity. Since PM and SO₂ emissions are dominated by industrial processes, a decrease is shown during August when industrial activities depict reduced intensity.

NM VOC emissions in Cyprus are dominated by solvent use and traffic. The resulting diurnal profile yields two maxima during the day; the first one in the early morning and the second one in the afternoon. Regarding the daily variation, a small increase is shown from Monday to Friday, whilst there is an important reduction during the weekends.

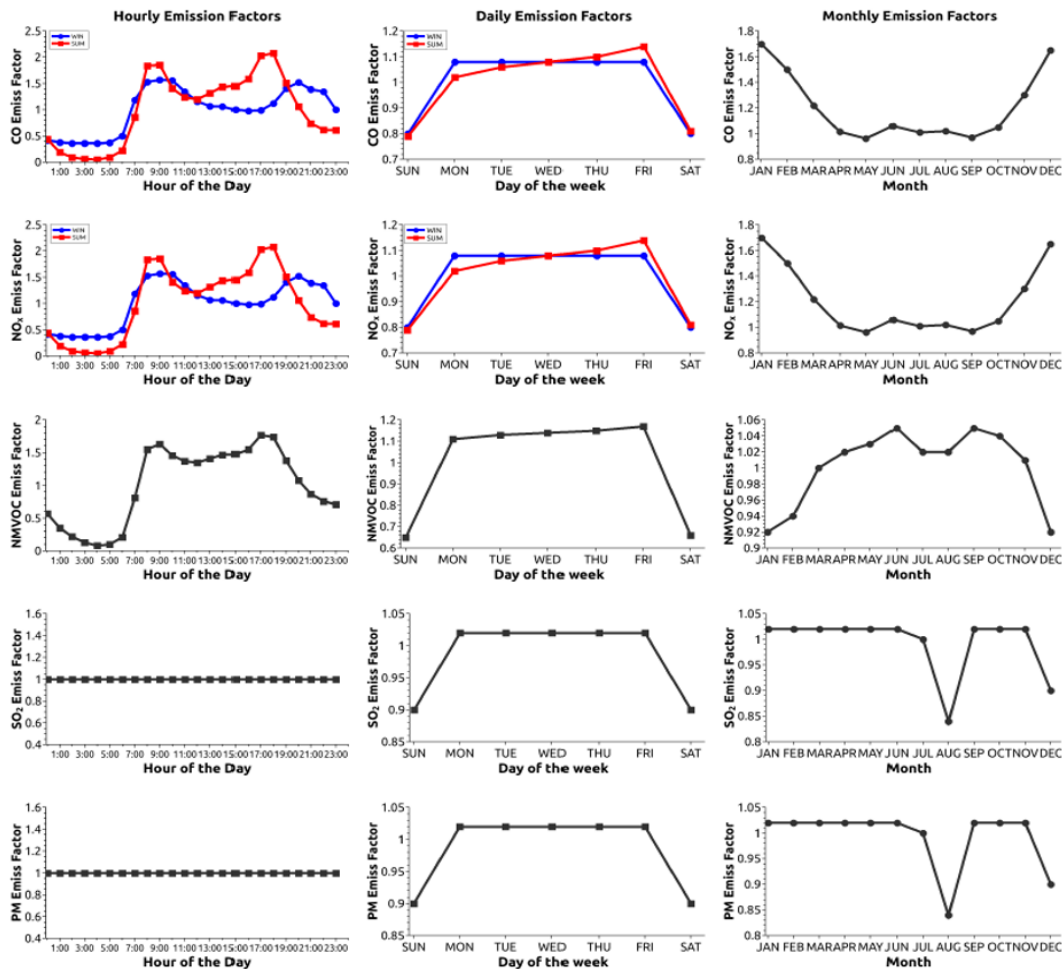


Fig. 1.4-6: Hourly (left), daily (centre), and monthly (right) emission factors for CO, NO_x, NMVOC, SO₂, and PM (from top to bottom).

1.4.5. Model performance

An up-to-date, fine spatial (1×1 km) resolution emission inventory for the island of Cyprus was implemented in the context of **WP6 (Task 6.2.a)** of the EMME-CARE project, to be used as input data for the regional air quality modelling with WRF/Chem. The temporal variation of the emission inventory in the model is scaled to include hourly intra- and inter-day (day-of-the-week and month-of-the-year) variations of anthropogenic emissions.

The implementation of diurnal cycles in the emissions is necessary in order to resolve the NO_x diurnal variation at the urban sites. The EDGAR simulation is severely limited in the representation of NO_x mixing ratios throughout the day because of the absence of diurnal variations in the applied emissions. In particular, the constant emission rate during the night and the absence of photochemistry can result in slightly higher modelled NO_x mixing ratios during the night. NO_x mixing ratios are reduced during daytime due to the intense photochemistry and the higher boundary layer height. During summer, the NO_x emission diurnal profile also yields a morning and an afternoon maximum. The peak in NO_x emissions occurs about 4 hours earlier compared to the winter period.

The potential of the model to reproduce the magnitude and diurnal profile of the NO_x mixing ratios at the urban sites, is of a great importance since they are both linked with the O₃ mixing ratios at these locations. Ozone-related air quality directives are based on specific hours of the day, during which peak ozone concentrations occur and the population is exposed to outdoor air pollution. Therefore, it is equally important to examine the effect of the emission inventories on the diurnal profile of O₃,

especially near densely populated areas. Local dust resuspension caused mainly by wind erosion from local crop-land contributes to elevated PM_{2.5} concentrations during the summer period. More than half of crop-lands in Cyprus are usually planted in November and harvested in April-May, leaving the land bare during the summer. There are significant differences in the spatial distribution of PM_{2.5} emissions in the EDGAR and newly implemented emission inventories.

Local emissions and decreased photochemistry result in higher NO_x mixing ratios during the winter period. The large differences between the EDGAR and HiRes emission inventories in the total amount of emitted NO_x, have an important impact on the NO_x mixing ratios near locations with anthropogenic activity. In addition, the incorporation of diurnal variation in the NO_x emissions lead to better representation of the diurnal profile of NO_x mixing ratios in urban areas, and hence, to improved performance by the HiRes inventory. The HiRes inventory includes the early morning and afternoon peaks in NO_x emissions. Thus, the abrupt decreases in O₃ mixing ratios which occur at the same time will be captured in the HiRes simulation. Since the ability of the model to reproduce the NO_x diurnal cycle is essential for the O₃ chemistry simulation at the urban sites, where population is exposed to air pollution, the diurnal variability of the anthropogenic emissions must be included in emission inventories, in order to enable the use of atmospheric chemistry models to properly assess air quality and its impacts in a meaningful way, and to be effective tools for policy making. The results of this work have been published in Georgiou et al. (2020 and 2022).

1.4.6. Emission analysis system

Enhanced by a boost project on emissions with ARIA technologies, CARE-C scientists developed in-house capacity on inventory development systems utilizing ground based and satellite data. The process consists of the following cornerstone components:

Data Collection and training tools:

General methodology for Emission Inventory work

ARIA Data Web Platform => for collection of industrial activity data

TREFIC model => for traffic emission calculations (bottom-up approach)

Access DB => for structuring and homogenising the emission inventory

EMEX => for visualising and analysing the content of the emission inventory

AriaCity Everywhere (traffic emissions using open data on traffic)

Methodology on stationary sources:

Large Point Sources (LPS)

The Cyl team identified and processed national data from the Department of Labour Inspection on large point sources in the island. The information includes the thermodynamics parameters (height, diameter, speed, temperature) for certain sources. EPRTR LPS database was used for Cyprus to demonstrate how to process emission data for dispersion modelling. Information on the capacity of power plants in the northern part of Cyprus was scarce.

Area sources

Cyl prepared the Activity report from the Department of Labour Inspection which provides annual emissions for different (sub)sectors for the preparation of the gridded inventory for area sources, for the identification of different sources of GIS data (Cyl DB, CLC, National GIS providers, GE...) to be used for spatial distribution of emissions.

Mobile sources

Training sessions were conducted on the TREFIC software allowing to compute emissions from the road traffic sector by providing information on vehicle fleet and the traffic flow on the road network. Data related to fleet and fuel data were collected:

- Fleet file: the department of transport provides the Cyprus vehicle fleet data for the years 1990-2019. The different macro-categories (PC, HDV, LDV, 2W) are considered and divided into sub-categories (fuel types, euro standards and size distribution)
- Fuel consumption: total fuel consumption for road transport for the years 1990-2019
- Mean mileage by vehicle category: data on annual mean mileage per vehicle category.
- Monthly fuel sales: fuel sales for road transport for December 2019.
- As the information related to traffic countings on the Cyprus road network was not available, a statistical approach was used to estimate road traffic emissions with the “AriaCity Everywhere (ACE)” tool. This tool uses the following approach:
 - Extracts Road network anywhere on earth from Open Street Map (OSM)
 - Analyzes road network characteristics (lanes, speed limits, density etc.)
 - Builds a random forest model from a global open data traffic counts DB + local data
 - Estimates traffic flow on road network
 - Simulates traffic-related emissions with the TREFIC model

Different methodologies for preparing the road traffic emission inventory for Cyprus were discussed during the project. For consistency with the other sectors, the final emission file for road traffic is based on the total emissions reported by the Labour of Inspection for road traffic. Spatial disaggregation was thereafter made with the output (fuel consumption) from the “Aria City Everywhere” calculation which included open data on traffic flow and moreover the traffic counting available from the “Open Transport Map” project (best available data). The road links in the northern part of Cyprus were included in this calculation (OSM data), and the emissions in the northern part were estimated by comparing fuel consumption in the northern and the southern part of Cyprus resulting from the ACE calculation.

Gridded inventory development

For the preparation of a national emission inventory the following steps were followed:

- Start from total emissions declared for Cyprus in the Labour of Inspection annual report for year 2019
- Select best available GIS data for spatial distribution of total emissions for each sector/subsector (select from Cyl postgres DB and national GIS DB/Corine Land Cover).
- Add northern part for main emission activities related to Power Plants and Road Traffic.
- Prepare emission files in ARIA emission manager format (POINT, LINE, AREA emission file formats). Convert NFR to SNAP source classification system.
- Run ARIA Emission Manager module for obtaining gridded, speciated hourly emission files in netcdf format for the Cyl dispersion modelling.
- The following data were available and used:
 - Emission database: Cyprus National Informative Inventory which is prepared on an annual basis by the department of Labour of inspection at the Ministry of Labour, Welfare and Social Insurance. The tabular NFR emission data for year 2019 was used in combination with the bottom-up inventory for Large Point sources for the same year.
 - Cartography: GIS data available at Cyprus Institute (Corine Land Cover, GIS data from earlier inventory work (postgres DB...))
 - Thematic maps/Spatial proxies: mostly not available. The collection of metadata and/or spatial data to use as proxy could be a main source of improvement for future spatial disaggregation of emissions on Cyprus (spatial population and employment data, land use data, type of activity and annual production at industrial and agricultural, sites, livestock numbers etc.)

- Time Modulations: EDGAR (Emissions Database for Global Atmospheric Research). Can be replaced with local data if/when available.
- The different processing steps in the EMISSION MANAGER script for preparing model-ready emission files for the dispersion model:
 - species split and NMVOC & PM speciation: the EMISSION MANAGER SPICE module, split the emissions of aggregated species in the input files into more detailed target chemical species according to the SAPRC99 chemical mechanism and the aero3 PM module; this is performed with sector/fuel-specific speciation profiles;
 - spatialization and “pemtim” file) creation: the base pemtim (extension ptm0) files are thereafter generated from the speciated client files using the modules TRLGSP (point sources), TRLCRS (area sources) and TRLLIN/LIGREC (line sources). For area sources, the TRLCRS module can further perform spatial disaggregation on the target grid by using gridded proxy layers previously prepared with GIS
 - species selection: using the REDSPE module, redundant species in the emission files can be eliminated; the reduced “pemtims” in the output (extension red) contain only the “target species” selected;
 - time modulation: using CRTEMP module, the mass emitted by each source is disaggregated into a series of hourly emission values for the chosen simulation period, by using yearly (12 months), weekly (7 days) and daily (24 hours) modulation profiles; the modulated pemtims are created (extension. mdl);
 - pemtims merge & translation to model-ready format: the MPEM2FARM and PEM2GRID modules creates the diffemi.nc file (netCDF format), containing total gridded hourly emissions for the selected time period from all sources in the inventory. The current inventory uses a 0.01° grid resolution (~1km).

Trend analysis

Satellite data have been used to investigate trends in emission fluxes of nitrogen oxides at regional and global scale in the framework of the META-Sat ESA project. We utilize a global atmospheric model to apply the methodology outlined in [Lamsal et al \(2011\)](#) regarding the identification of the relationship between NO_x emissions and NO_x vertical column density (VCD) in our area of interest. To achieve this objective two simulations are performed with the EMAC global Earth system model: one with the original EDGAR HTAP v2.2 global emissions as provided by the Joint Research Center (JRC) for the year 2010 (base case simulation thereafter referred to as EMACREF) described in Janssens-Maenhout et al., (2015) and the second with a 30% perturbation in the emission fluxes of each grid cell covering an area of 0.1x0.1 degrees (EMAC30). The ratio between the difference in NO_x emissions ($\Delta E/E = 30\%$) and the resulting difference in modelled NO_x VCD ($\Delta\Omega/\Omega$) is defined as a factor (β) that describes in a linearized way the nonlinear nature of the relationship between emissions and concentrations of NO₂ in the atmosphere. We propose the use of the inverse beta factor to the one in Lamsal et al. (2011) given that $\Delta E/E$ in the beta calculation procedure is a constant number and we keep it in the denominator position (instead of the numerator position of Lamsal et al. (2011) and assess the differences in the nominator $\Delta\Omega/\Omega$ being smaller or larger than the emission perturbation. Thus, when the beta factor is less than 1 ($\beta < 1$) the result denotes that an emission reduction of 30% causes -a less than- 30% change in NO_x VCD indicating a more efficient NO_x loss, a result of higher OH levels in low-NO_x environments. When $\beta > 1$ enhanced NO_x levels suppress OH levels resulting in a relative increase in NO₂ columns larger than the perturbation in emissions (< 30%).

Subsequently, the β factor can be used to update emission inventories based on emission trend analysis derived from satellite-observed VCDs. Emissions of year y can be thus derived from emissions of year x based on the changes of VCDs derived from satellite measurements between year x and y. We update the emissions of 2010, last available monthly EDGAR-HTAP emissions, to 2015, based on trend analysis derived from tropospheric NO₂ columns from the Ozone Monitoring Instrument onboard

NASA's EOS Aura mission homogenised in the framework of the EU FP7 Quality Assurance for Essential Climate Variables project ([Boersma et al., 2017](#)).

After deriving 'new' updated emission fluxes for 2015 we compare the trend produced from the satellite observations with the trend denoted from the official EDGAR NO_x. The simulations were performed with a global model, namely the numerical model system ECHAM/MESSy Atmospheric Chemistry (EMAC). The ECHAM/MESSy Atmospheric Chemistry (The EMAC model is a numerical chemistry and climate simulation system that includes sub-models describing tropospheric and middle atmosphere processes and their interaction with oceans, land and human influences ([Jöckel et al., 2010](#)). It uses the second version of the Modular Earth Submodel System (MESSy2) to link multi-institutional computer codes. The core atmospheric model is the 5th generation European Centre Hamburg general circulation model (ECHAM5, [Roeckner et al., 2006](#)). For the present study we applied EMAC (ECHAM5 version 5.3.02, MESSy version 2.54.0.2) in the T42L31-resolution, i.e. with a spherical truncation of T42 (corresponding to a quadratic Gaussian grid of approx. 2.8 by 2.8 degrees in latitude and longitude) with 31 vertical hybrid pressure levels up to 10 hPa, with roughly 22 levels in the troposphere. The dynamical circulation was nudged using Newtonian relaxation ([Jeuken et al., 1996](#); [Jöckel et al., 2006](#)) towards the ERA-interim reanalysis ([Berrisford et al., 2011](#)) of European Centre for Medium-Range Weather Forecasts (ECMWF) to reproduce the actual day-to-day meteorology in the troposphere. Atmospheric chemistry is calculated using the module MECCA ([Sander et al., 2011](#)) In this study we simulated two years (2009-2010), with the first year used as spin-up time. Atmospheric chemistry is calculated using the module MECCA ([Sander et al., 2011](#))

Our baseline emission information comes from the inventories from EDGAR-HTAP (Emission Database for Global Atmos. Res. for Hemispheric Transport of Air Pollution) Version 2, compiled by the European Commission, Joint Research Center (JRC)/Netherlands Environmental Assessment Agency. This dataset includes emissions of gaseous pollutants such as sulphur dioxide (SO₂), NO_x, CO, non-methane volatile organic compounds (NMV OCs) and ammonia (NH₃) and particulate matter with carbonaceous speciation (PM₁₀; PM_{2.5}; black carbon, BC; and organic carbon, OC) from anthropogenic and biomass burning sectors. PM_{2.5} is a subset of PM₁₀ and includes BC, OC, SO₄²⁻, NO₃⁻, crustal material, metal, and other dust particles. The dataset used in this study is available in 0.1o × 0.1o emission grid maps for the year 2010 and can be downloaded from the EDGAR JRC website per year (that includes monthly variation), per substance, and per sector.

Regarding satellite information, the data produced in the framework of the Quality Assurance for Essential Climate Variables (QA4ECV) project are used and specifically the NO₂ vertical column density (VCD) datasets that cover our base simulation year (2015) from OMI (EOS-Aura) extending from 2004 – 2017 ([Boersma et al., 2017](#)). We produced a post-processing script that helps visualise the data (in ncl format). The VCD data for 2010 (left plot per month) and 2015 (right plot per month) for each month are shown in Figure 1a and used as a spatial mapping of the changes in the column intensity of NO₂ as captured by satellites (units 10¹⁵ molecules per grid cell area). While differences in summer time tropospheric VCD are not so clearly evident (qualitatively speaking) from the maps, wintertime reduction from 2010 to 2015 is clearly seen over China, Europe, several coastal zones in Middle East (home to large urban conglomerates and/or industrial activity) as well as North West US. Indicatively, two maps representing the difference in OMI NO₂ VCD between 2015 and 2010 for the months of January and July are depicted in Figure 1.4.7 b (expressed as VCD₂₀₁₅-VCD₂₀₁₀).

It has been found that summer-time uncertainties of the trend analysis process are lower to winter period, owing to the fast photochemical reaction rates that lead to a reduced lifetime of NO₂ in the atmosphere. NO₂ trends (from 2010 to 2015) are positive for Europe and North Africa (enhancement of

emissions in 2015 compared to 2010), while India has lower emissions fluxes in 2015. Over Asia there are two distinct zones with opposite emission trend signs (North-East and South-West areas) with the south-west region following the negative trend pattern of the Indian region (**Fig. 1.4-7**). The most notable positive trend (increase in emission fluxes) occurs for the months of September, October and November over all regions with significant anthropogenic emissions. Other than that, the trend mapping is very complex with positive and negative signs throughout the year with the only stand-out pattern that of a negative trend over Asia and India during the first half of the year and a positive trend in the second half. The scaled emissions and satellite derived trend factors can be used by the international community to assess the impact on regional and global air pollution as well as to apply to other available emission inventories.

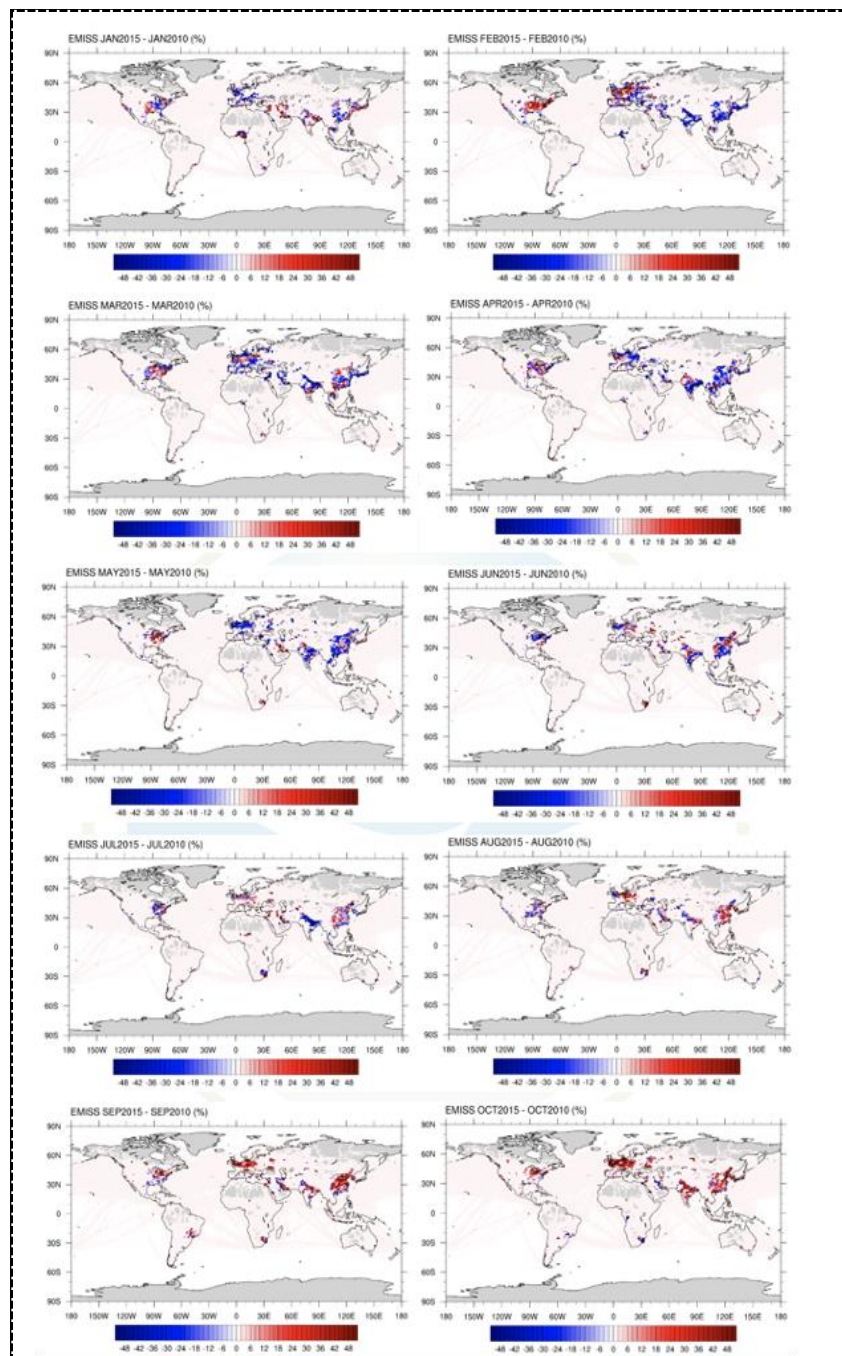


Fig. 1.4-7: Difference in percentage between updated and original mean monthly emissions where the scaling configuration is based on the b70_OMI factor (30% reduction at OMI overpass time).

2. Key aspects of the implementation of the project

2.1. Autonomy, Decision-making

- This task was run as part of WP6 coordinated by MPG. Partners had frequent meetings and teleconferences for co-supervised students
- We have done more than scheduled in the DoA by inverting emissions of CH₄, NO₂, SO₂ and NH₃ in task 6.3b. However, the inversion of CO emissions planned is being updated with a new high resolution version of the LMDZ INCA model and we waited for the new version of the TROPOMI CO data, hence this work will be presented in the next periodic report
- No separate deliverables on HR issues.

2.2. Complementary funding

- ESA EO4Society project with contribution of CEA, MPG and CYI.
- EDU4Climate project coordinated by CYI
- ACCEPT Norwegian Funds project coordinated by Cyl
- AQ-SERVE Integrated Project, Research and Innovation Foundation, Cyprus
- META-SAT ESA PECS project coordinated by Cyl

3. Strategy for the upcoming period

- The strategy foreseen for the CoE in the upcoming period is to perform an **inversion of CO₂ and CO using the global model LMDZ INCA and TROPOMI CO** products and to develop a regional inversion configuration of the CHIMERE regional model
- The main target is to arrive at an integrated emission inverse modelling system dealing with all the species listed in the report and to update the results annually
- Communication about the work has been performed via social media and press releases on key publications
- No bottleneck is foreseen

4. Publications

Georgiou, G. K., Christoudias, T., Proestos, Y., Kushta, J., Pikridas, M., Sciare, J., Savvides, C., and Lelieveld, J.: Evaluation of WRF-Chem model (v3.9.1.1) real-time air quality forecasts over the Eastern Mediterranean, *Geosci. Model Dev.*, 15, 4129–4146, <https://doi.org/10.5194/gmd-15-4129-2022>, 2022

Kushta, J., Georgiou, G.K., Lelieveld, J. (2021). Timely Update of Emission Inventories with the Use of Satellite Data. In: Mensink, C., Matthias, V. (eds) *Air Pollution Modeling and its Application XXVII. ITM 2019. Springer Proceedings in Complexity*. Springer, Berlin, Heidelberg. https://doi.org/10.1007/978-3-662-63760-9_10

Peng, S., Lin, X., Thompson, R. L., Xi, Y., Liu, G., Hauglustaine, D., et al. (2022). Wetland emission and atmospheric sink changes explain methane growth in 2020. *Nature*, 612(7940), 477–482. <https://doi.org/10.1038/s41586-022-05447-w>

Rey-Pommier, A., Chevallier, F., Ciais, P., Broquet, G., Christoudias, T., Kushta, J., Hauglustaine, D., and Sciare, J.: Quantifying NO_x emissions in Egypt using TROPOMI observations, *Atmos. Chem. Phys.*, 22, 11505–11527, <https://doi.org/10.5194/acp-22-11505-2022>, 2022.

- Rey-Pommier, A., Chevallier, F., Ciais, P., Kushta, J., Christoudias, T., Bayram, I. S., and Sciare, J.: Detecting nitrogen oxide emissions in Qatar and quantifying emission factors of gas-fired power plants - A four-years study, *EGUsphere* [preprint], <https://doi.org/10.5194/egusphere-2023-1024>, 2023.
- T. Lauvaux et al. ,Global assessment of oil and gas methane ultra-emitters. *Science* **375**,557-561(2022).DOI:10.1126/science.abj4351
- Tibrewal, K., P. Ciais, M. Saunois, A. Martinez, X. Lin, Z. Deng, F. Chevallier, C. Giron, C. Albergel, K. Tanaka, P. Patra, A. Tsuruta, B. Zheng, D. Belikov, Y. Niwa, R. Janardanan, S. Maksyutov, A. Segers, Z. A. Tzompa-Sosa, P. Bousquet, J. Sciare.: Assessment of national methane emissions from oil, gas and coal sectors across inventories and atmospheric inversions. *Communications Earth & Environment* [under review].

5. References

- Van Damme, M., Clarisse, L., Franco, B., Sutton, M.A., Erisman, J.W., Kruit, R.W., Van Zanten, M., Whitburn, S., Hadji-Lazaro, J., Hurtmans, D. and Clerbaux, C., 2021. Global, regional and national trends of atmospheric ammonia derived from a decadal (2008–2018) satellite record. *Environmental Research Letters*, 16(5), p.055017.
- Sutton, M.A., Reis, S., Riddick, S.N., Dragosits, U., Nemitz, E., Theobald, M.R., Tang, Y.S., Braban, C.F., Vieno, M., Dore, A.J. and Mitchell, R.F., 2013. Towards a climate-dependent paradigm of ammonia emission and deposition. *Philosophical Transactions of the Royal Society B: Biological Sciences*, 368(1621), p.20130166.
- Steffen Beirle et al., Pinpointing nitrogen oxide emissions from space. *Sci. Adv.* 5, eaax9800(2019).DOI:10.1126/sciadv.aax9800
- Hauglustaine, D.A., Hourdin, F., Jourdain, L., Filiberti, M.A., Walters, S., Lamarque, J.F. and Holland, E.A., 2004. Interactive chemistry in the Laboratoire de Météorologie Dynamique general circulation model: Description and background tropospheric chemistry evaluation. *Journal of geophysical research: Atmospheres*, 109(D4).
- Fioletov, V.E., McLinden, C.A., Griffin, D., Abboud, I., Krotkov, N., Leonard, P.J., Li, C., Joiner, J., Theys, N. and Carn, S., 2023. Version 2 of the global catalogue of large anthropogenic and volcanic SO₂ sources and emissions derived from satellite measurements. *Earth System Science Data*, 15(1), pp.75-93.
- Theys, N., Fioletov, V., Li, C., De Smedt, I., Lerot, C., McLinden, C., Krotkov, N., Griffin, D., Clarisse, L., Hedelt, P. and Loyola, D., 2021. A sulfur dioxide Covariance-Based Retrieval Algorithm (COBRA): application to TROPOMI reveals new emission sources. *Atmospheric Chemistry and Physics*, 21(22), pp.16727-16744.
- McDuffie, E.E., Smith, S.J., O'Rourke, P., Tibrewal, K., Venkataraman, C., Marais, E.A., Zheng, B., Crippa, M., Brauer, M. and Martin, R.V., 2020. A global anthropogenic emission inventory of atmospheric pollutants from sector-and fuel-specific sources (1970–2017): an application of the Community Emissions Data System (CEDS). *Earth System Science Data*, 12(4), pp.3413-3442.
- Zheng, B., Geng, G., Ciais, P., Davis, S.J., Martin, R.V., Meng, J., Wu, N., Chevallier, F., Broquet, G., Boersma, F. and van der A, R., 2020. Satellite-based estimates of decline and rebound in China's CO₂ emissions during COVID-19 pandemic. *Science Advances*, 6(49), p.eabd4998.
- Osipov, S., Chowdhury, S., Crowley, J.N., Tadic, I., Drewnick, F., Borrmann, S., Eger, P., Fachinger, F., Fischer, H., Predybaylo, E. and Fnaiss, M., 2022. Severe atmospheric pollution in the Middle East is attributable to anthropogenic sources. *Communications Earth & Environment*, 3(1), p.203.

- Koukouli, M.E., Theys, N., Ding, J., Zyrichidou, I., Mijling, B., Balis, D. and van der A, R.J., 2018. Updated SO₂ emission estimates over China using OMI/Aura observations. *Atmospheric Measurement Techniques*, 11(3), pp.1817-1832.
- Qu, Z., Henze, D.K., Li, C., Theys, N., Wang, Y., Wang, J., Wang, W., Han, J., Shim, C., Dickerson, R.R. and Ren, X., 2019. SO₂ emission estimates using OMI SO₂ retrievals for 2005–2017. *Journal of Geophysical Research: Atmospheres*, 124(14), pp.8336-8359.
- Ukhov, A., Mostamandi, S., Krotkov, N., Flemming, J., Da Silva, A., Li, C., Fioletov, V., McLinden, C., Anisimov, A., Alshehri, Y.M. and Stenchikov, G., 2020. Study of SO₂ pollution in the Middle East using MERRA-2, CAMS data assimilation products, and high-resolution WRF-Chem Simulations. *Journal of Geophysical Research: Atmospheres*, 125(6), p.e2019JD031993.
- Yin, Y., Chevallier, F., Ciais, P., Bousquet, P., Saunois, M., Zheng, B., et al. (2021). Accelerating methane growth rate from 2010 to 2017: leading contributions from the tropics and East Asia. *Atmos. Chem. Phys.*, 17.
- Locatelli, R., Bousquet, P., Saunois, M., Chevallier, F., & Cressot, C. (2015). Sensitivity of the recent methane budget to LMDz sub-grid-scale physical parameterizations. *Atmospheric Chemistry and Physics*, 15(17), 9765–9780. <https://doi.org/10.5194/acp-15-9765-2015>
- Peng, S., Lin, X., Thompson, R. L., Xi, Y., Liu, G., Hauglustaine, D., et al. (2022). Wetland emission and atmospheric sink changes explain methane growth in 2020. *Nature*, 612(7940), 477–482. <https://doi.org/10.1038/s41586-022-05447-w>
- Deng, Z., Ciais, P., Tzompa-Sosa, Z. A., Saunois, M., Qiu, C., Tan, C., Sun, T., Ke, P., Cui, Y., Tanaka, K., Lin, X., Thompson, R. L., Tian, H., Yao, Y., Huang, Y., Lauerwald, R., Jain, A. K., Xu, X., Bastos, A., ... Chevallier, F. (2022). Comparing national greenhouse gas budgets reported in UNFCCC inventories against atmospheric inversions. *Earth System Science Data*, 14(4), 1639–1675. <https://doi.org/10.5194/essd-14-1639-2022>
- Crippa, M., Guizzardi, D., Muntean, M., Schaaf, E., Lo Vullo, E., Solazzo, E., Monforti-Ferrario, F., Olivier, J., & Vignati, E. (2021). EDGAR v6.0 Greenhouse Gas Emissions. European Commission, Joint Research Centre (JRC) [Dataset]. <https://data.jrc.ec.europa.eu/dataset/97a67d67-c62e-4826-b873-9d972c4f670b>
- Höglund-Isaksson, L., Gómez-Sanabria, A., Klimont, Z., Rafaj, P., & Schöpp, W. (2020). Technical potentials and costs for reducing global anthropogenic methane emissions in the 2050 timeframe – results from the GAINS model. *Environmental Research Communications*, 2(2), 025004. <https://doi.org/10.1088/2515-7620/ab7457>
- O'Rourke, P. R., Smith, S. J., Mott, A., Ahsan, H., McDuffie, E. E., Crippa, M., Klimont, Z., McDonald, B., Wang, S., Nicholson, M. B., Feng, L., & Hoesly, R. M. (2021). CEDS v_2021_04_21 Release Emission Data. In Community Emissions Data System. <https://doi.org/10.5281/zenodo.4741285>
- Scarpelli, T. R., Jacob, D. J., Grossman, S., Lu, X., Qu, Z., Sulprizio, M. P., Zhang, Y., Reuland, F., Gordon, D., & Worden, J. R. (2022). Updated Global Fuel Exploitation Inventory (GFEI) for methane emissions from the oil, gas, and coal sectors: evaluation with inversions of atmospheric methane observations. *Atmospheric Chemistry and Physics*, 22(5), 3235–3249. <https://doi.org/10.5194/acp-22-3235-2022>
- International Energy Agency. (2021). IEA Data and statistics. IEA. <https://www.iea.org/data-and-statistics/data-sets>
- United States Environmental Protection Agency. (2021). Global Greenhouse Gas Emissions Data. USEPA. <https://www.epa.gov/ghgemissions/global-greenhouse-gas-emissions-data>